SANDIA REPORT

SAND2003-1591
Unlimited Release
Printed May, 2003

Process-Based Quality Tools to Verify Cleaning and Surface Preparation

John A. Emerson, Rachel K. Giunta, David E. Reedy, David P. Adams, Paul A. Lemke, and Neville R. Moody

Prepared by
Sandia National Laboratories
Albuquerque, New Mexico 87185 and Livermore, California 94550

Sandia is a multiprogram laboratory operated by Sandia Corporation,
a Lockheed Martin Company, for the United States Department of Energy's
National Nuclear Security Administration under Contract DE-AC04-94AL85000.

Sandia National Laboratories

Issued by Sandia National Laboratories, operated for the United States Department of Energy by Sandia Corporation.

Available to DOE and DOE contractors from
U.S. Department of Energy
Office of Scientific and Technical Information
P.O. Box 62
Oak Ridge, TN 37831

Telephone: (865)576-8401
Facsimile: (865)576-5728
E-Mail: reports@adonis.osti.gov
Online ordering: http://www.doe.gov/bridge

Available to the public from
U.S. Department of Commerce
National Technical Information Service
5285 Port Royal Rd
Springfield, VA 22161

Telephone: (800)553-6847
Facsimile: (703)605-6900
E-Mail: orders@ntis.fedworld.gov
Online order: http://www.ntis.gov/help/ordermethods.asp?loc=7-4-0#online

SAND2003-1591
Unlimited Release
Printed May 2003

Process-Based Quality Tools to Verify Cleaning and Surface Preparation

John A. Emerson and Rachel K. Giunta
Organic Materials Department

David E. Reedy
Materials Mechanics Department

David P. Adams
Thin Film, Vacuum and Packaging Department

Paul A. Lemke
Manufacturing Science and Technology Center

Sandia National Laboratories
P.O. Box 5800
Albuquerque, NM 87185-0958

Neville R. Moody
Microsystems and Materials Mechanics
Sandia National Laboratories
P.O. Box 969
Livermore, CA 94551-9401

Abstract

A test method, the Tensile Brazil Nut Sandwich (TBNS) specimen, was developed to measure mixed-mode interfacial toughness of bonded materials. Interfacial toughness measured by this technique is compared to the interfacial toughness of thin film adhesive coatings using a nanoindentation technique. The interfacial toughness of solvent-cast and melt-spun adhesive thin films is compared and found to be similar. Finally, the Johnson-Kendall-Roberts (JKR) technique is used to evaluate the cleanliness of aluminum substrates.

Table of Contents

List of Figures 5

List of Tables 7

1. Fracture specimen to measure mixed-mode interfacial toughness of bonded materials 8

  1.1. Background 8

  1.2. Tensile Brazil Nut Sandwich (TBNS) specimen 9

  1.3. TBNS specimen toughness measurements 10

2. Melt Spun Films 11

  2.1. Background 11

  2.2. Materials and Procedures 12

    2.2.1. Materials 12

    2.2.2. Nanoindentation 13

    2.2.3. Fracture Mechanics Testing 14

  2.3. Results and Discussion 15

    2.3.1. Mechanical Properties 15

    2.3.2. Thin Film Delamination 31

    2.3.3. Fracture Energy Analysis 32

3. Contact Mechanics 37

  3.1. Background 37

    3.1.1. Overview of Present Work 38

    3.1.2. Overview of JKR Contact Mechanics 39

  3.2. Materials and Procedures 42

    3.2.1. Contact Mechanics Experiment 42

    3.2.2. Preparation of Epoxy Elastomers 43

    3.2.3. Preparation and Modification of Aluminized Glass 43

  3.3. Results and Discussion 43

    3.3.1. Adhesion Hysteresis Parameter 46

    3.3.2. Significant Surface Contamination 48

  3.4. Summary 48

4. Acknowledgments 49

5. Appendix A. Validation of the method used to insert an initially sharp crack52

6. Appendix B. G calibration for the TBNS specimen 55

Distribution: 59

List of Figures

Figure 1.1. Tensile Brazil Nut Sandwich (TBNS) specimen. 9

Figure 1.2. G_c of an epoxy/SAM-coated aluminum interface vs. applied mode mixity (75% bromine mixed monolayer SAM coating). 11

Figure 2.1. (a) Phase angle versus displacement curve generated during the indenter approach, showing the point of surface contact. (b) Variation in near surface properties obtained by using different definitions of the point of contact, illustrating the sensitivity of polymers to this definition. 14

Figure 2.2. (a) Load vs. contact depth of melt-spun epoxy films, illustrating the portion of the curve that corresponds to the epoxy film, the sputtered aluminum film, and the underlying silicon dioxide surface. (b) Load, measured by nanoindenter, as a function of contact depth in melt-spun epoxy films. 16

Figure 2.3. Modulus (a) and hardness (b) as a function of contact depth for samples spun for 60 minutes at 1000 rpm. 17

Figure 2.4. Modulus (a) and hardness (b) as a function of contact depth for samples spun for 60 minutes at 3000 rpm. 18

Figure 2.5. Modulus (a) and hardness (b) as a function of contact depth for samples spun for 60 minutes at 4500 rpm. 19

Figure 2.6. Modulus (a) and hardness (b) as a function of contact depth for samples precured for 5 minutes at 70°C. 21

Figure 2.7. Modulus (a) and hardness (b) as a function of contact depth for samples precured for 15 minutes at 70°C. 22

Figure 2.8. Modulus (a) and hardness (b) as a function of contact depth for samples precured for 25 minutes at 70°C. 23

Figure 2.9. Near-surface modulus (a) and hardness (b) as a function of precure time for three spin rates. 24

Figure 2.10. Near-surface modulus (a) and hardness (b) as a function of spin rate for three precure times. 25

Figure 2.11. Epoxy film thickness as a function of spin rate for three precure times. 26

Figure 2.12. Modulus (a) and hardness (b) as a function of epoxy film thickness for three precure times. 27

Figure 2.13. The relationship derived by Marsh (1963) shows a linear relationship exists between yield strength and properties for glasses and glassy polymers. 28

Figure 2.14. Modulus (a) and hardness (b) as a function of contact depth for samples with different processing steps performed. 30

Figure 2.15. (a) Wrinkles and (b) telephone cord blisters that formed when stressed overlayers were deposited on the melt spun films........................32

Figure 2.16. (a) Measurement location and (b) schematic of a telephone cord blister profile. 34

Figure 2.17. (a) Schematic of blister cross-section showing moments and loads from which (b) phase angles of loading for circular and telephone cord (straightwall) blisters were calculated as a function of effective driving force. From Hutchinson and Suo (1992)..36

Figure 2.18. The total stored energy in melt spun films is greater than the total stored energy that triggered interfacial fracture in spin cast films. 37

Figure 3.1. Schematic of a polymer adhesive/substrate interface in the absence (left) and presence (right) of surface contamination. In the latter case, the contaminant molecules can displace the polymer from the interface resulting in a degradation of the adhesive bond strength. Adapted from [27]............38

Figure 3.2. Schematic illustration of the JKR contact mechanics experiment, where *P* is the load, *a* is the lens contact radius, δ is the penetration depth of the lens, and *R* is the radius of curvature of the lens..................................40

Figure 3.3. Typical curves obtained from a single JKR loading experiment. In all cases, the symbols represent the data points and the solid lines trace the fits to the data for an epoxy lens against a γ-aminopropylsilane-modified silicon wafer. (a) Contact radius cubed vs. applied load; (b) displacement vs. contact radius; (c) displacement vs. applied load. Adapted from [45].........41

Figure 3.4. Block diagram of JKR system used for contact mechanics studies. .42

Figure 3.5. Chemical structure of epoxy resin and curing agent used to make contact mechanics lenses..43

Figure 3.6. JKR loading and unloading curves of higher-modulus epoxy elastomers in contact with (a) air-plasma cleaned aluminum and (b) hexadecane-contaminated aluminum...44

Figure 3.7. JKR loading and unloading curves of lower-modulus epoxy elastomers in contact with (a) air-plasma cleaned aluminum, and (b) hexadecane-contaminated aluminum...45

Figure 3.8. Illustration of lines fit to JKR data for calculation of adhesion hysteresis parameter, H...47

Figure 3.9. Photograph of epoxy lens in contact with a substrate that has been contaminated with a significant amount of hexadecane..............................48

Figure 5.1. Load vs. load-point displacement for two TBNS specimens that had a crack starter composed of a 23-mm ODTS SAM and either a 15-mm or 20-mm long Teflon tape applied on top of the SAM...53

Figure 5.2. Load vs. load-point displacement measured during the pre-cracking of a TBNS specimen (load held fixed at about 75% of the failure load until the interface opens)...54

Figure 6.1. Nondimensional *G* calibration function *f* for a diametrally-loaded aluminum/epoxy TBNS specimen (h/R=0.2, R_L/R=0.8, α=0.90, β=0.21) as a function of *a/R* and θ (in curve fits, x=*a/R* and y=*f*). 56

Figure 6.2. Nondimensional *G* calibration function *f* for a diametrally-loaded aluminum/epoxy TBNS specimen (h/R=0.02, a/R=0.91, R_L/R=0.8, α=0.90, β=0.21) as a function of and θ (in curve fits, x=θ and y=*f*). 57

Figure 6.3. Nondimensional *G* calibration function *f* for the +/30° loading about the crack plane (a/R=0.0197, R_L/R=0.8, α=0.90, β=0.21) as a function of *a/R* (in curve fits, x=*a/R* and y=*f*). 58

List of Tables

Table 2.1: Processing study sample matrix 13

Table 2.2. Properties of melt spun Epon828/T403 on aluminized glass substrates as a function of spin rate and cure time. 20

Table 2.3. Comparison of Solvent versus Neat Film Properties..........................20

Table 2.4. The effect of process techniques on properties of melt spun Epon 828/T403. 31

Table 2.5. Average film thickness, heights and blister half-widths, delamination stresses, residual stresses, and fracture energies from telephone cord blisters in melt spun Epon 828/T403 films. 34

Table 3.1. Adhesion Hysteresis Parameter, *H* 47

1. Fracture specimen to measure mixed-mode interfacial toughness of bonded materials

1.1. Background

Interfacial toughness is a material property that can be used to predict when an existing interfacial crack will advance. A detailed discussion of interfacial fracture mechanics theory can be found in several excellent references.[1, 2] One aspect of interfacial fracture mechanics that distinguishes it from traditional linear elastic fracture mechanics is the role of mode mixity. Asymmetries with respect to the interface are responsible for the inherently mixed mode condition found at the tip of an interfacial crack. Both normal and shear stresses are present on the interface ahead of the crack tip, and in general the ratio of these stresses changes with distance from the crack tip. The level of mode mixity (defined as the arctangent of the ratio of shear stress to normal stress at a fixed distance l in front of the crack tip in the region dominated by the stress singularity) depends on the elastic properties and the body's overall geometry and loading. According to current thought, resistance to interfacial crack propagation is most conveniently specified in terms of critical energy release rate G_C versus the mode mixity $\psi_{r=l}$. The fracture criterion for interfacial cracking is then defined by

$$G=G_c(\psi_{r=l}) \qquad \textbf{Equation 1.1}$$

where $G_c(\psi_{r=l})$ is the mode mixity dependent interfacial toughness. An interface crack that is subjected to mode mixity $\psi_{r=l}$ advances when the energy release rate for crack extension G equals the critical value associated with that mode mixity, $G_c(\psi_{r=l})$. There is experimental evidence, for at least relatively weak interfaces, that G_C increases substantially with increasing $|\psi_{r=l}|$.[3, 4] Note that the interfacial fracture toughness of a strongly bonded, epoxy/solid interface can be orders of magnitude greater than the reversible work of adhesion measured using contact-mechanics based methods (e.g., JKR). Furthermore the interfacial toughness of a mm-thick epoxy bond can be much greater than that of a micron-thick epoxy film because bulk energy dissipation is limited by the thickness of the thin film. Consequently the interfacial toughness measured using bonded joints with mm-thick epoxy bonds will typically exceed that measured by the nanoindentation of micron-thick epoxy layers even though the interfaces are nominally identical.

The goal of the present effort is to develop an easy to use interfacial fracture test that can measure toughness of a mm-scale bonded joint over a relatively large range mode mixity. In particular, the test should 1) use a specimen that can be readily fabricated and pre-cracked, 2) only require the measurement of failure load (i.e., no compliance or crack length measurement), and 3) permit the applied mode mixity to be changed by simply changing the loading points. One fracture specimen that fulfills these requirements is the recently developed Tensile Brazil Nut Sandwich (TBNS) specimen first introduced Kuhl, et al.[5] Our adaptation of TBNS test is described below. The accuracy of TBNS test method has been improved with the development of a technique for inserting a sharp starter crack of known length as well as the development of a more accurate calibration function for determining G_c from the failure load, initial crack length, and the position of the loading points. Also presented are some preliminary TBNS test results that illustrate both the dependence of G_c on mode mixity and the consistency of the measured toughness data. The TBNS test method is complementary to the JKR and nanoindentation methods, and provides a method for measuring the interfacial toughness of a bonded material with a mm-scale bond. This data can be used to help design and qualify bonded components to meet performance requirements.

1.2. Tensile Brazil Nut Sandwich (TBNS) specimen

The Tensile Brazil Nut Sandwich (TBNS) fracture specimen consists of two semicircular aluminum disks bonded together by a 0.5-mm thick epoxy layer (Figure 1.1). Each 50.8-mm diameter bonded disk is 10.2-mm thick. The specimen is loaded via pins inserted through one of the sets of the opposing 3.2-mm diameter holes that are positioned along a 20.3-mm radius circle. The applied mode mixity can be changed by using different pairs of loading-holes, and a 90 degree variation in applied crack-tip mode mixity is possible. The ability to easily adjust the applied mode mixity over a wide range of potential values is a substantial advantage over other common types of interfacial fracture specimens.

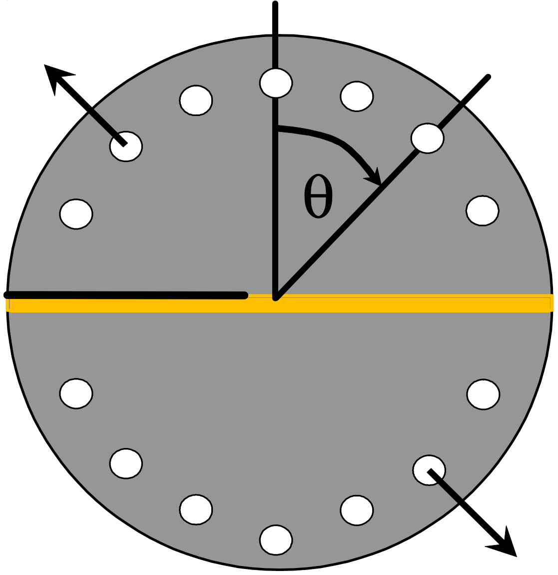

Figure 1.1. Tensile Brazil Nut Sandwich (TBNS) specimen.

Each TBNS specimen is fabricated separately. Small spacers are bonded to the ends of one of the semi-circular aluminum disks to define the epoxy layer thickness, and the other adherend is subsequently positioned on top. Teflon tape is then applied to the edges of the specimen to contain the epoxy resin. The TBNS specimen is placed in an open cavity RTV fixture to aid handling, and a syringe with a small diameter tip is inserted through the tape to fill the bond cavity with epoxy. Finally the RTV fixture that contains the specimen is placed in an oven to cure the epoxy.

Crack growth is unstable in the TBNS specimen. Crack length is not independently measured during the test and is assumed known. In addition, meaningful and consistent data requires an initially sharp crack, and methods that insert a relatively blunt crack (e.g. use of Teflon tape to define the initial crack) are suspect. For these reasons, the method used to insert a sharp pre-crack of known length is crucial to the success of this specimen. In the method used here, a 23-mm long ODTS SAM (octadecyltrichlorosilane self assembled monolayer) is applied to the bonding surface of one of the semicircular disks, and an 18-mm long Teflon tape is applied on top of the SAM. The 5-mm long portion of the SAM that extends beyond the tape insures that an initially sharp arrested crack can be generated. Instrumented tests showed that the crack arrests at the end of the SAM during the pre-cracking step. See Appendix A for further details and results that verify the method used to insert the initial crack.

The specimen is loaded at a crosshead displacement rate of 0.02 mm/s by means of a load train that utilizes a chain linkage that connects to a pair of loading-holes. Tests were conducted with $\psi_{r=10\mu m}$ of 2°, -12°, -26°, and -42° by loading diametrically opposing loading-holes with the upper loading-hole located at 0°, -20°, -40°,and -60°, respectively (Figure 1.1). A $\psi_{r=10\mu m}$ of 2° was also generated by loading the two loading-holes closest to the crack plane (i.e., +/-30° from the crack plane). This loading configuration is particularly useful when pre-cracking a specimen since the G level is seven times higher than that generated when the specimen is subject to the same load, but loaded using diametrally opposed 0° loading-holes. Failure load is the only measured quantity in a TBNS fracture test. A calibration function, which depends on failure load, initial crack length, and the position of the loading points, is used to determine interfacial toughness and the associated crack-tip mode mixity. More than thirty detailed finite element analyses were performed to establish the required TBNS specimen calibration. See Appendix B for details.

1.3. TBNS specimen toughness measurements

A limited number of TBNS specimens were tested to illustrate the dependence of G_c on mode mixity. The TBNS data was also compared with Asymmetric Double Cantilever Beam Sandwich (ADCBS) data to verify the toughness measurements. A visual examination of all failed specimens revealed that the crack runs along the interface and there is no indication of cohesive failure.

TBNS specimens with a 0.5-mm thick epoxy bond and a 75% bromine-terminated SAM-coated aluminum/epoxy interface were tested. These tests complement a larger experimental effort aimed at assessing how variations in surface interactions affect interfacial toughness,[6] and this is why a SAM coating was applied to the aluminum surface. The adherends were 6061-T6 aluminum and the SAM was applied on a highly polished aluminum surface (root means square surface roughness, R_q, of < 0.1 micron). The adhesive was an EPON 828 (Shell) epoxy resin, cross-linked with an aliphatic polyethertriamine (T-403, Huntsman Chemical). A 100/43 by weight epoxy to cross-linker mix ratio was used and the epoxy was cured for 5 days at 50°C. The TBNS specimens were stored in a desiccator prior to testing, and all tests were conducted at room temperature and in laboratory air.

Figure 1.2 plots G_c data for an applied mode mixity ranging from $\psi_{r=10\mu m}$=2° to $\psi_{r=10\mu m}$=-42°. The overall trend of the G_c vs. $\psi_{r=10\mu m}$ data is consistent with that observed by others; G_C increases substantially with increasing $|\psi_{r=10\mu m}|$.[3, 4] Eight tests were run with a $\psi_{r=10\mu m}$=2° loading. Six of these samples were loaded using the two loading-holes closest to the crack plane (i.e., +/-30° from the crack plane, referred to as a symmetric loading) while the other two where loaded using the diametrically opposed 0° loading holes (Figure 1.1, referred to as the diametral loading). Although the load required to generate the same G values is 2.6 times greater for the diametral loading, the measured G_c values are similar. Also note that the measurements were made using two sets of specimens that were fabricated at different times, demonstrating the reproducibility of the fabrication process. The average G_c value for $\psi_{r=10\mu m}$=2° is 37 J/m^2, with a coefficient of variation of 14% (the 95% confidence interval about the mean is 37+/- 4 J/m^2). Asymmetric Double Cantilevered Beam Sandwich (ADCBS) specimens were used to measure the interfacial toughness of essentially similar 70% and 80% bromine-terminated SAM-coated aluminum/epoxy interface in another recent study.[6] These ADCBS results are also plotted in Figure 1.2. The TBNS and ADCBS data are in good agreement and consequently confirm the toughness measurements.

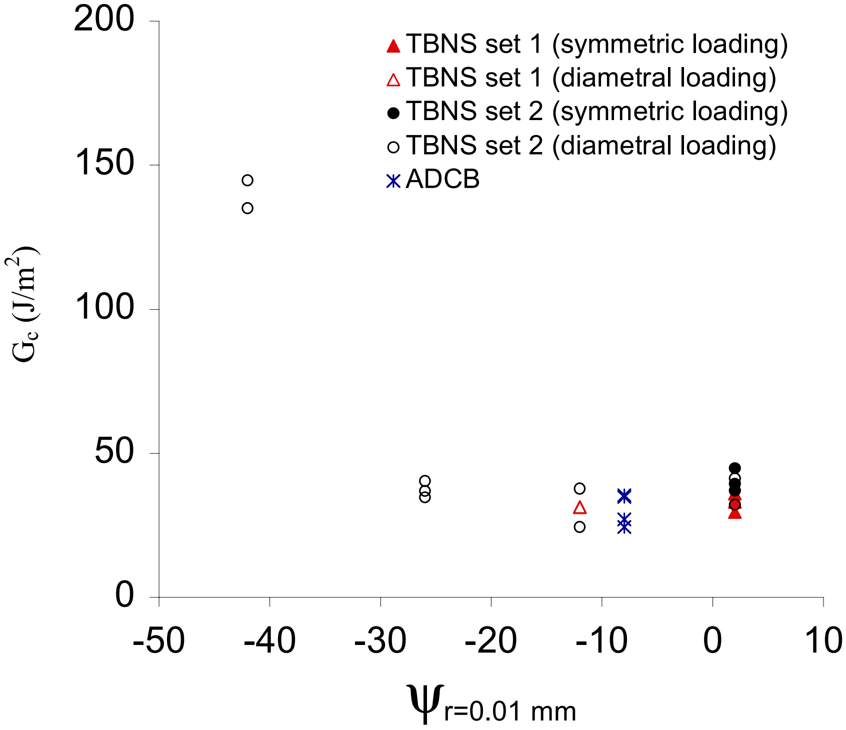

Figure 1.2. G_c of an epoxy/SAM-coated aluminum interface vs. applied mode mixity (75% bromine mixed monolayer SAM coating).

2. Melt Spun Films

2.1. Background

Adhesion is an important factor in controlling the performance and reliability of thin polymer films on metal substrates. Advances in nanoindentation test techniques allow us to measure elastic modulus and hardness, and estimate yield strengths. However, our understanding of failure in these systems is limited by a lack of established test techniques for very thin layer systems. Traditional test techniques such as double cantilever beam sandwich samples[7] often require relatively thick films while peel tests are dominated by plastic energy contributions as the film is bent.[8] In addition, it is difficult to maintain uniform film thickness in traditional sandwich geometries when bonds are less than one micron thick. The work of Bagchi et al.,[9, 10] and more recently the work by Kriese and coworkers[11, 12] and Zhuk et al.[13] shows that these limitations can be overcome for testing thin metal and polymer films by deposition of a relatively hard, highly stressed overlayer. This overlayer uniformly stresses the film and under the right conditions triggers delamination and interfacial failure. In this portion of the program, we used nanoindentation and stressed overlayer tests to study processing effects on deformation and interfacial fracture properties of thin melt spun epoxy films on aluminum substrates.

Previous studies[14] of thin polymer film adhesion to aluminum substrates show a decrease in adhesive strength as the bondline decreases from 1000 to 0.01 µm. These films were prepared by spincoating a solvent-diluted epoxy/curing agent mixture. We speculated whether preferential segregation or adsorption of the material components might happen in the thinner films. To answer this question, we measured the hardness and elastic modulus of spin-on epoxy amine-cured thin films prepared by two techniques—solvent cast and neat. This work was done to remove any questions in sample preparation for further studies. It is easier to form thin films by solvent casting. However, to make thin adhesive joints that are void free, non-solvent systems are preferred. Nanoindentation techniques were used to measure the properties of films.

2.2. Materials and Procedures

2.2.1. Materials

Epon 828/T403 was chosen for study as the mechanical properties and structure are well characterized and complement applications.[7] It consists of a 100:46 ratio of Epon 828 resin and T403 hardener. In the first portion of this program (MS samples), the epoxy was melt spun onto aluminized glass substrates. The aluminized glass substrates provided a smooth uniform polymer-metal interface for assessing the effects of adhesion on properties and interfacial fracture. The two components were preheated to 70°C, mixed, and then precured at 70 ˚C for 5, 15, or 25 minutes. These film systems were spun to final thickness at 1000, 3000, or 4500 rpm under a heat lamp for 60 minutes. The substrate temperature was approximately 50°C. After spinning, the samples were cured at 50°C for 5 days. These samples provided a matrix to study spin rate and cure time effects on deformation and interfacial fracture properties.

In the second portion of this program (CL samples), as-machined 60612-T6 aluminum substrates were given a combination of an FPL etch, plasma clean, and primer coat. Thin epoxy films were spin-coated from toluene solution onto the aluminum substrates and analyzed by nanoindentation to study surface preparation effects on deformation and interfacial fracture properties. The processing matrix is given in Table 2.1. Details of the etching, cleaning, and priming steps are given below.

FPL Etch Procedure: Aluminum plates were immersed for 10 min into a 66°C solution that was (by weight):

1 part $Na_2Cr_2O_7{\cdot}2H_20$
10 parts sulfuric acid
30 parts deionized water

The plates were then rinsed with 50°C deionized water and oven dried at 50°C.

Plasma Cleaning: Plasma cleaning was performed using a Plasma-Preen 11-862 (Plasmatic Systems). The chamber was evacuated for several minutes and purged with argon at 2 SCFM for several minutes. The samples were then exposed to plasma for 7 min.

Priming: Heatcon BMS 5-89 was brushed on and air-dried at room temperature.

The epoxy films were then spin-coated onto the substrates at 1000 rpm for 30 seconds and cured at 50 ˚C for 7 days.

Table 2.1: Processing study sample matrix

	Process steps:		
Sample ID	**FPL etch**	**Plasma cleaning**	**Primer**
CL1	Yes	Yes	Yes
CL2	Yes	Yes	No
CL3	Yes	No	No
CL4	No	Yes	Yes
CL5	No	No	Yes
CL6	No	No	No
CL7	Yes	No	Yes
CL8	No	Yes	No

2.2.2. Nanoindentation

The elastic modulus and hardness values of the films were measured using the continuous stiffness measurement option on a Nano Indenter II™ with a Berkovich diamond indenter at a superimposed excitation frequency of 45 Hz and displacement of 3 nm.[15,16] Unlike metal and ceramic films, approach rate and point of surface contact have a strong effect on near surface polymer properties. Previous work[17] on this film system showed that an approach rate of 2 nm/s minimized kinetic effects. A systematic study of the relationship between near surface properties and point of contact was conducted as part of this program. The point of surface contact is defined by the deviation in the phase angle versus displacement curve generated during the indenter approach as shown in Figure 2.1(a). In metals and ceramics, near surface properties are relatively insensitive to where this point is chosen as long as it is beyond the point of inflection. In contrast, polymers are quite sensitive to where this point is chosen with high near surface properties obtained when the point of contact is defined well beyond the inflection to low surface properties when this point is taken just before the inflection, Figure 2.1(b). The optimum point of contact for polymers appears to be just after the inflection. Nevertheless there is still some small variability in near surface properties. Ten indentations were made on each sample to determine mechanical properties. All tests were conducted in air at 22˚C, well below the glass transition temperature of 68˚C. The approach rate was set at 2 nm/s and the point of surface contact was defined as occurring just after the inflection in the phase angle versus displacement curve during the indenter approach.

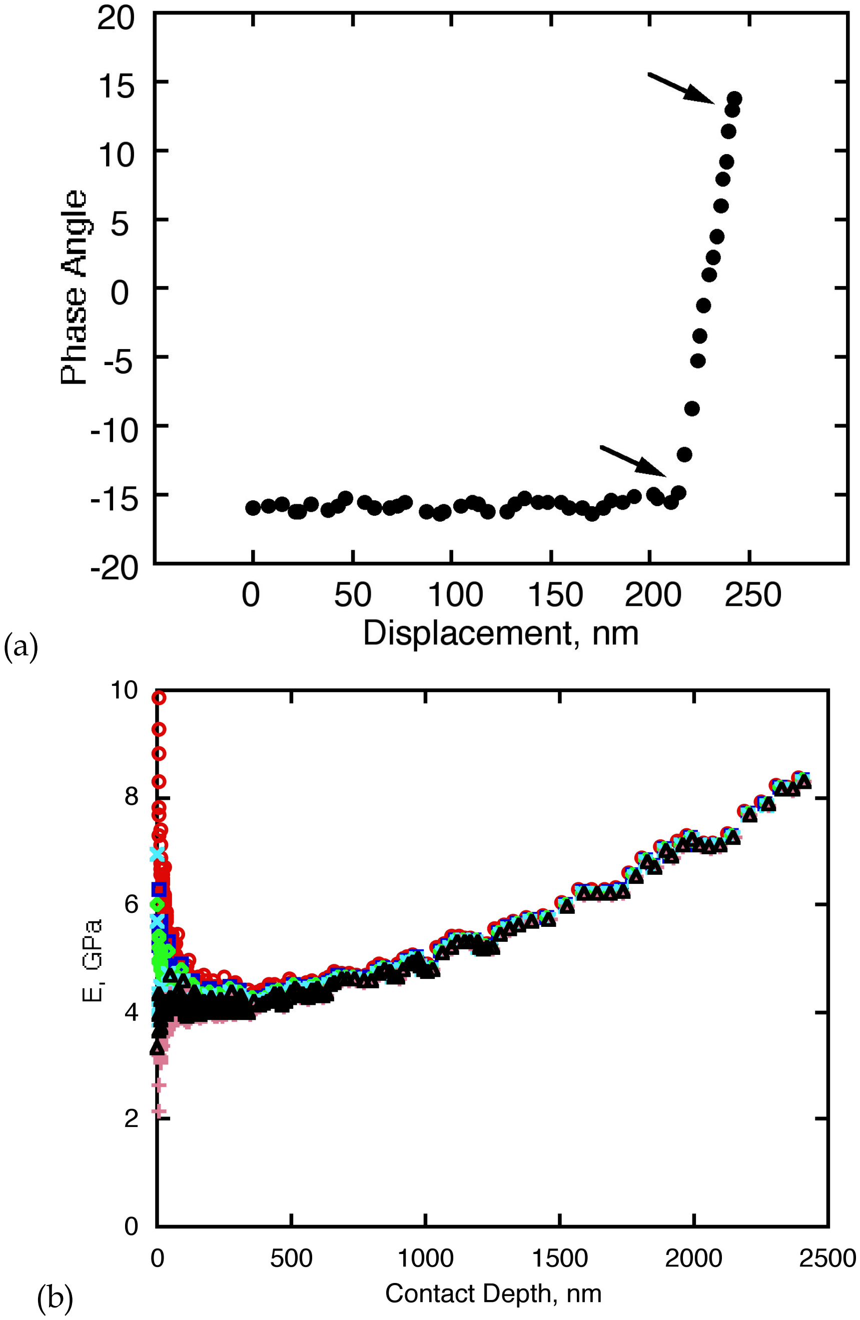

Figure 2.1. (a) Phase angle versus displacement curve generated during the indenter approach, showing the point of surface contact. (b) Variation in near surface properties obtained by using different definitions of the point of contact, illustrating the sensitivity of polymers to this definition.

2.2.3. Fracture Mechanics Testing

2.2.3.1. Stressed Overlayers and Nanoindentation

Additional stress from tungsten overlayers was required for testing thinner films. Tungsten overlayer deposition was accomplished by placing the epoxy films into a sputter deposition chamber, evacuating to 3×10^{-6} torr, backfilling with 2.5 mTorr argon gas, and sputter depositing tungsten at a rate of 0.2 nm/s to a final thickness of 220 nm. A companion silica wafer showed that deposition induced a compressive residual stress in the tungsten films of -2.2 GPa.

2.3. Results and Discussion

2.3.1. Mechanical Properties

Ten indentation tests were performed on each sample, generating load versus contact depth plots. Figure 2.2(a) shows two of these plots and how inflections in the plots correspond to features characterizing the epoxy films on aluminized glass substrate systems. The inflections at the epoxy to aluminum interface provide a measure of film thickness for each system. Select system AFM profiles verified the use of this approach. Curves for all film systems tested are given in Figure 2.2(b) and show there is significant variation in film thickness and mechanical response with variations in spin rate and precure time.

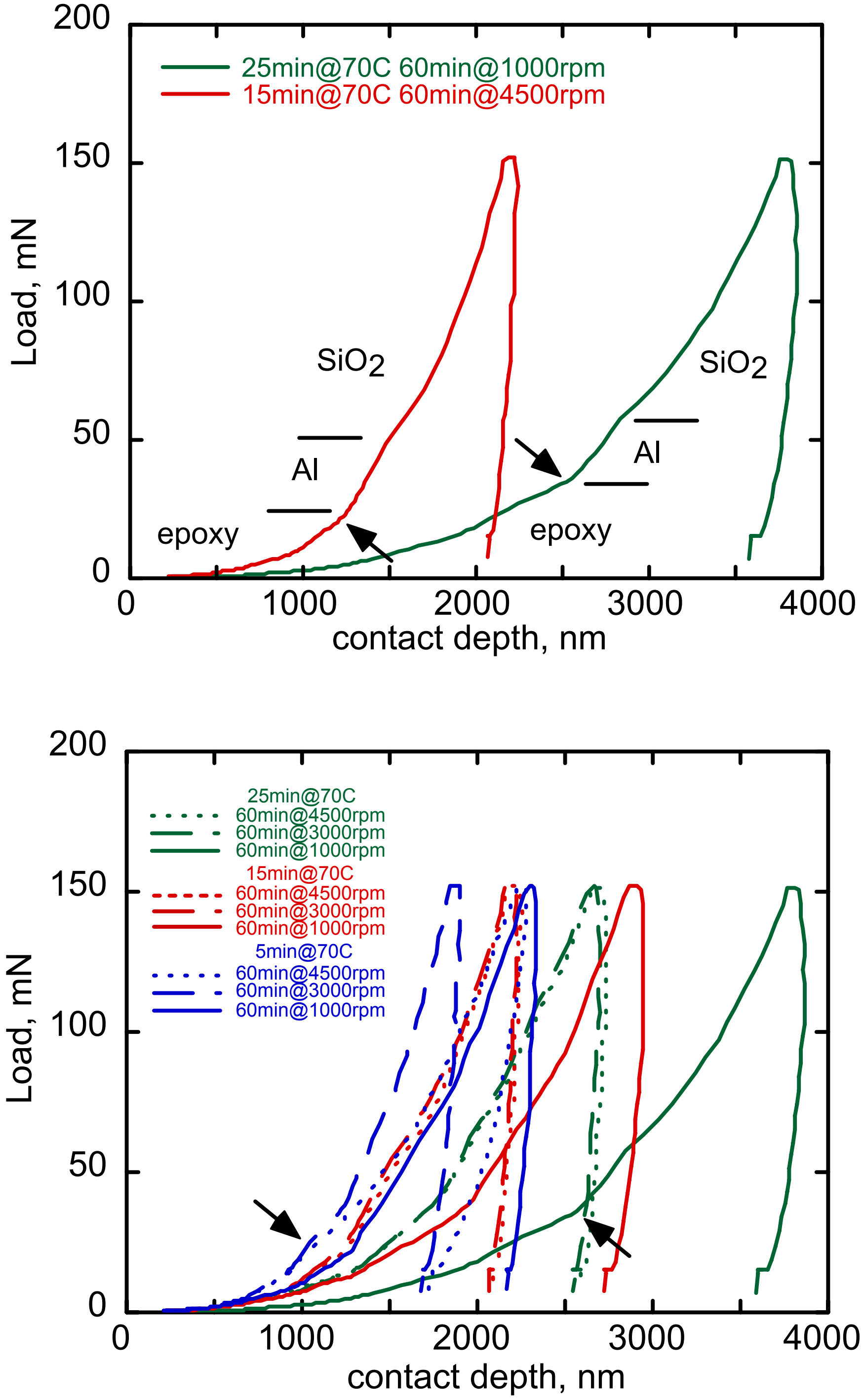

(a)

(b)

Figure 2.2. (a) Load vs. contact depth of melt-spun epoxy films, illustrating the portion of the curve that corresponds to the epoxy film, the sputtered aluminum film, and the underlying silicon dioxide surface. (b) Load, measured by nanoindenter, as a function of contact depth in melt-spun epoxy films.

Elastic modulus and hardness were obtained as a function of depth for each film as shown in Figure 2.3-Figure 2.5 for each spin rate as a function of precure time. In all cases, the shorter precure time leads to a higher modulus and hardness.

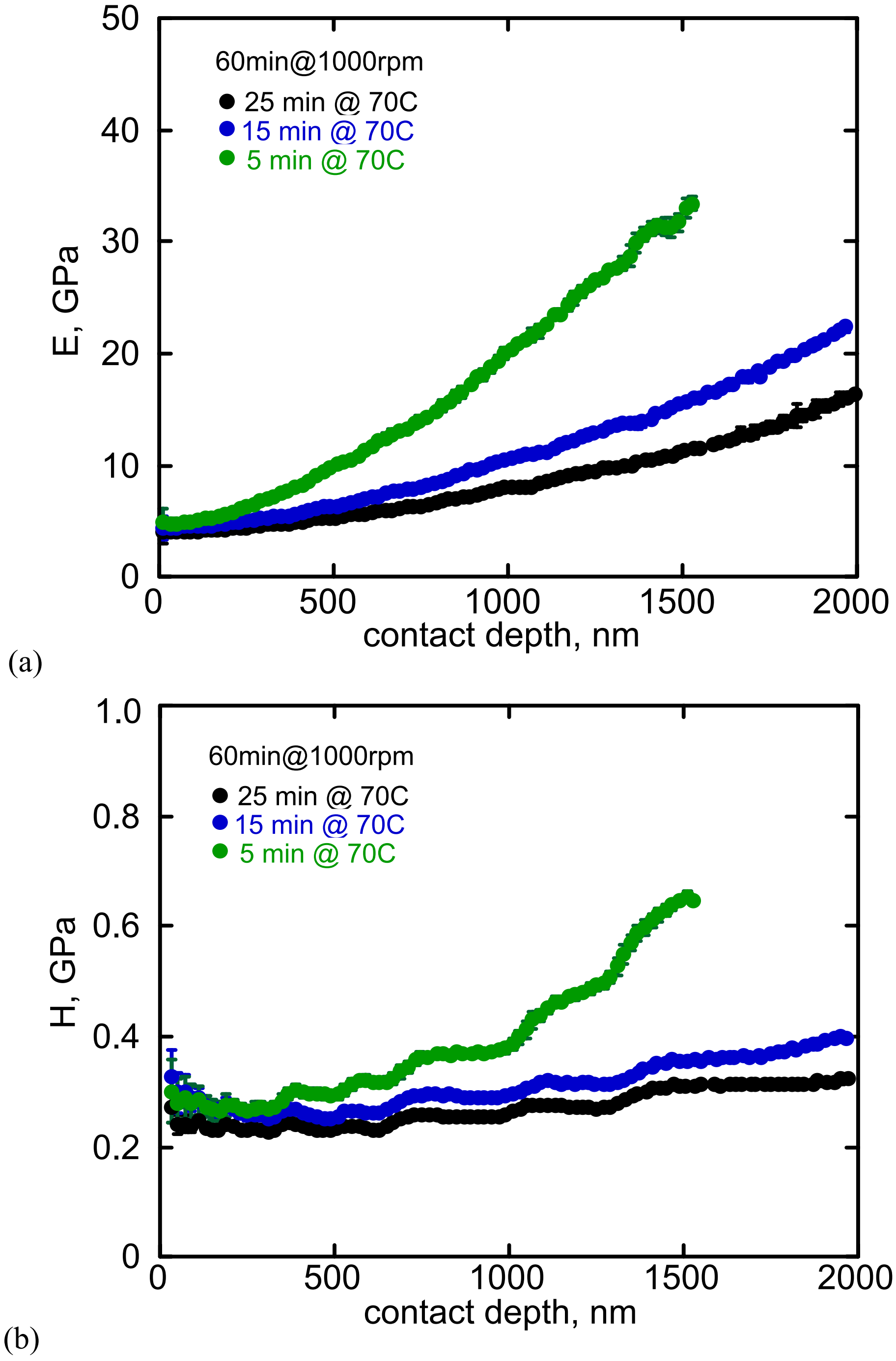

Figure 2.3. Modulus (a) and hardness (b) as a function of contact depth for samples spun for 60 minutes at 1000 rpm.

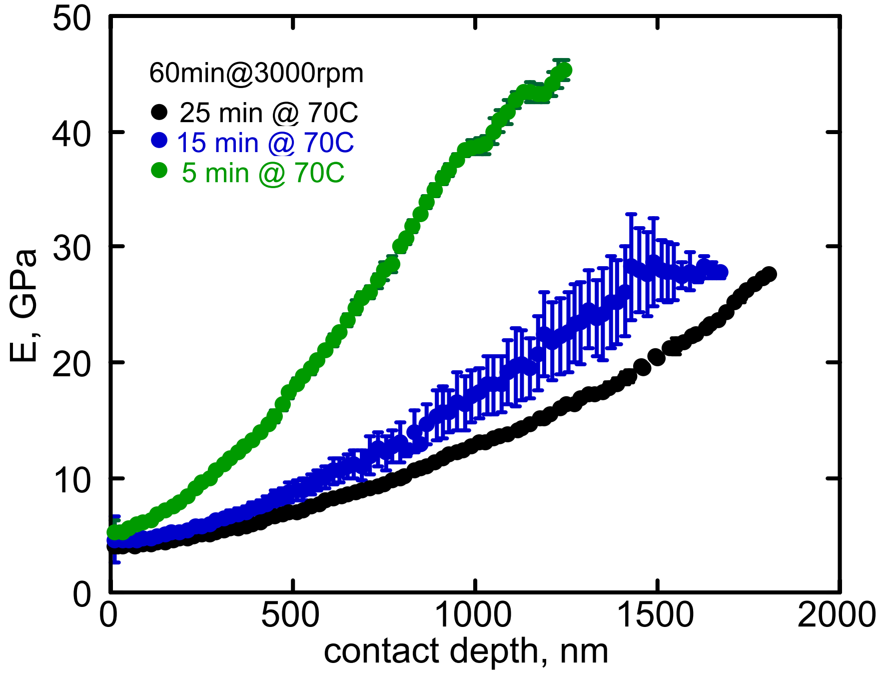

(a)

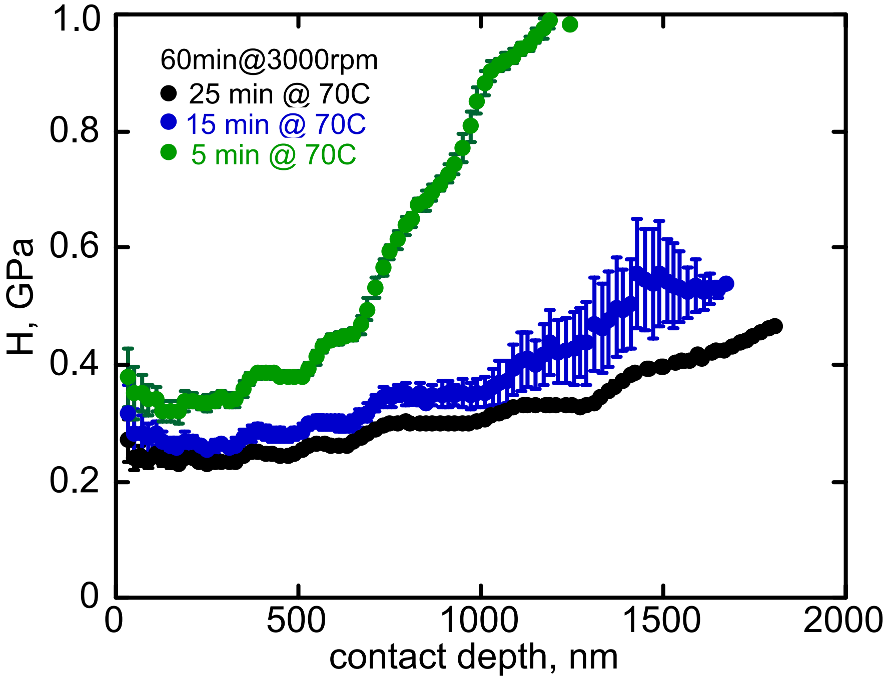

(b)

Figure 2.4. Modulus (a) and hardness (b) as a function of contact depth for samples spun for 60 minutes at 3000 rpm.

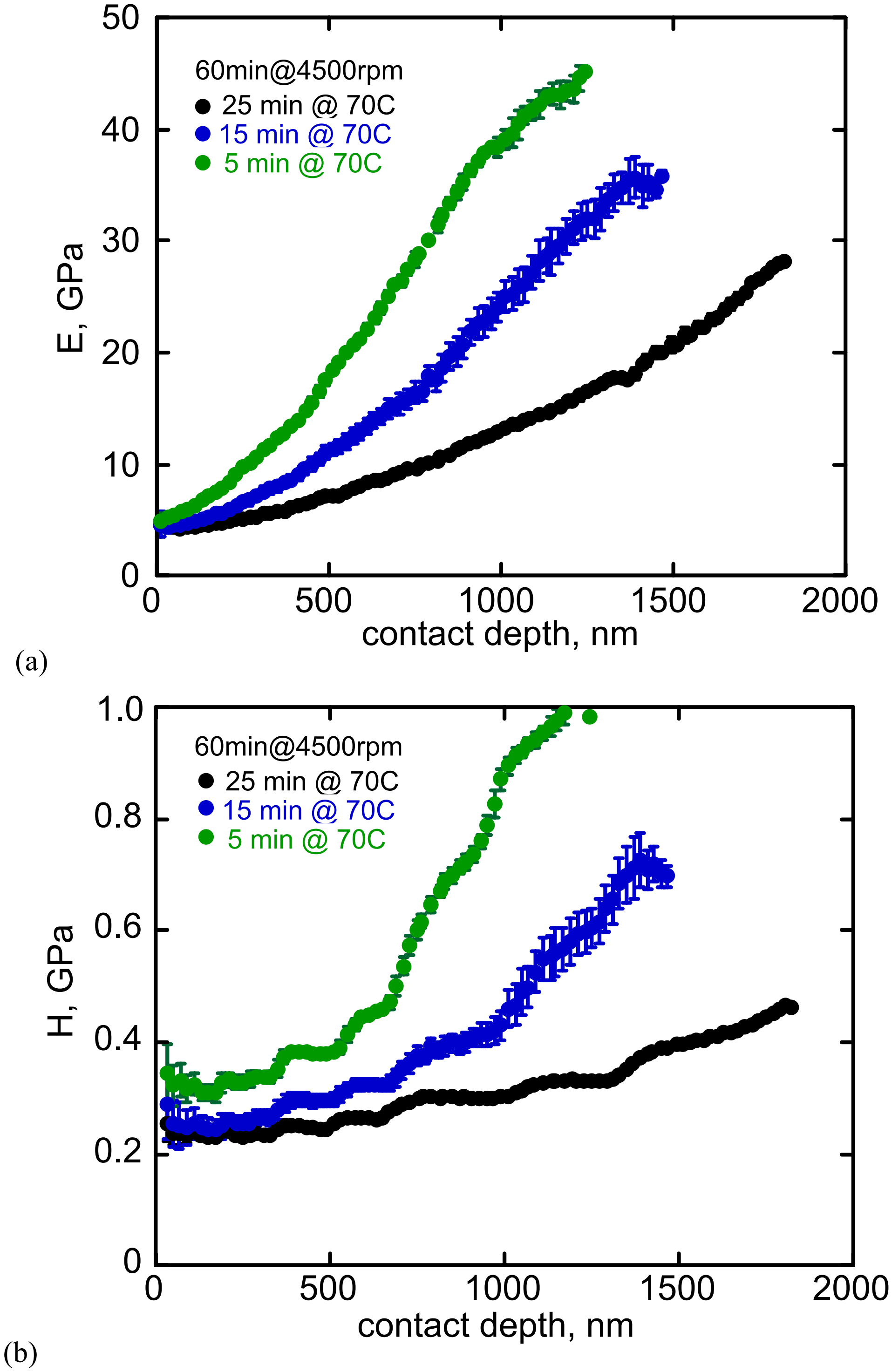

Figure 2.5. Modulus (a) and hardness (b) as a function of contact depth for samples spun for 60 minutes at 4500 rpm.

These data show that elastic modulus and hardness reach a plateau near the surface and maintain these values into the film before substrate effects begin to affect the measurements. The effect of the substrate on measured properties is more pronounced in thinner films, which are obtained from higher spin speeds. The film properties are summarized in Table 2.2.

Table 2.2. Properties of melt spun Epon828/T403 on aluminized glass substrates as a function of spin rate and cure time.

Sample	Time (min)	Spin Rate (rpm)	E (GPa)	H (GPa)	Yield Strength (MPa)	Thickness (μm)
MS1	25min@70°C	60min@1000rpm	4.04±0.22	0.25±0.02	105	2.55
MS2	25min@70°C	60min@3000rpm	4.11±0.14	0.25±0.02	113	1.80
MS3	25min@70°C	60min@4500rpm	4.30±0.21	0.24±0.02	114	1.50
MS4	15min@70°C	60min@1000rpm	4.44±0.32	0.30±0.04	147	1.29
MS5	15min@70°C	60min@3000rpm	4.56±0.28	0.29±0.04	171	1.06
MS6	15min@70°C	60min@4500rpm	4.55±0.45	0.26±0.04	130	1.04
MS7	5min@70°C	60min@1000rpm	4.83±0.36	0.29±0.04	115	1.93
MS8	5min@70°C	60min@3000rpm	5.69±0.37	0.36±0.04	133	1.26
MS9	5min@70°C	60min@4500rpm	5.58±0.30	0.33±0.04	141	1.24

The plateaus give an average near-surface modulus of 4.7 GPa and hardness for all films of 290 MPa. From these values a yield strength of 130 MPa was estimated for all films using the empirical relationship between hardness and yield strength of glasses and glassy polymers derived by Marsh.[18] These values are compared with the modulus, hardness, and yield strength of solvent-cast films in Table 2.3.

Table 2.3. Comparison of Solvent versus Neat Film Properties

	Average Film Modulus, GPa	Average Hardness, MPa	Average Yield Strength, MPa
Neat	4.7 ± 0.6	290 ± 40	130 ± 20
Solvent[19]	4.35	250	115

We found no measurable difference between the two sample preparation techniques. This is good news, because we were concerned about the following potential effects of sample preparation:

- Component separation because of differences in solubility
- Preferential surface absorption of individual components
- Competing surface interactions of the polymer components and the adsorbed solvent

The data presented in Figure 2.3-Figure 2.5 are given in Figure 2.6-Figure 2.8 for each precure time as a function of spin rate. Comparing the spin speeds for a given precure time, the modulus is lower for the samples spun at 1000 rpm, but no differences are observed overall for samples spun at 3000 vs. 4500 rpm. The same trend is observed when comparing the film hardness. This difference is attributed to the thicker film acquired when using a slower spin speed.

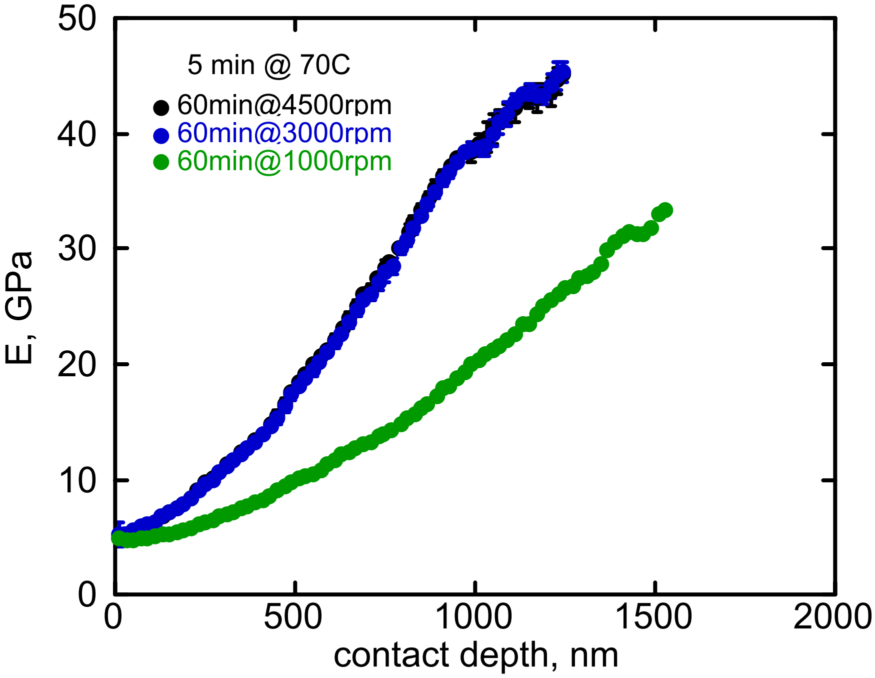

(a)

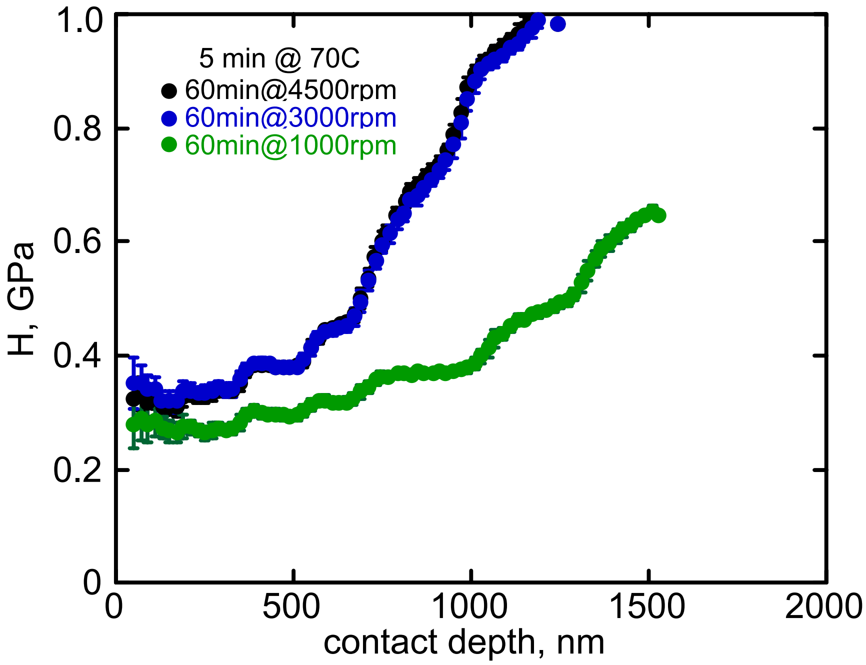

(b)

Figure 2.6. Modulus (a) and hardness (b) as a function of contact depth for samples precured for 5 minutes at 70°C.

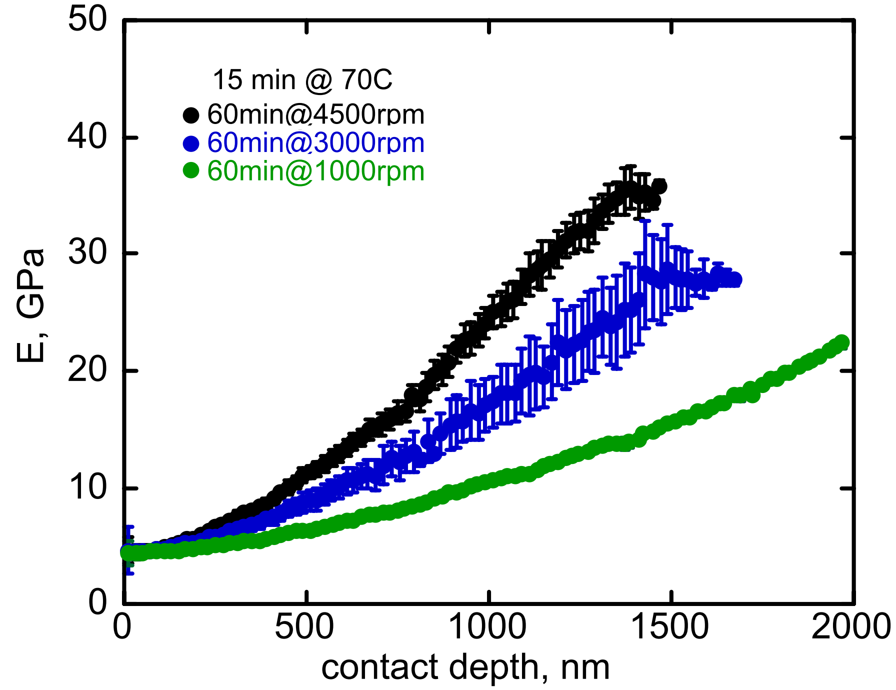

(a)

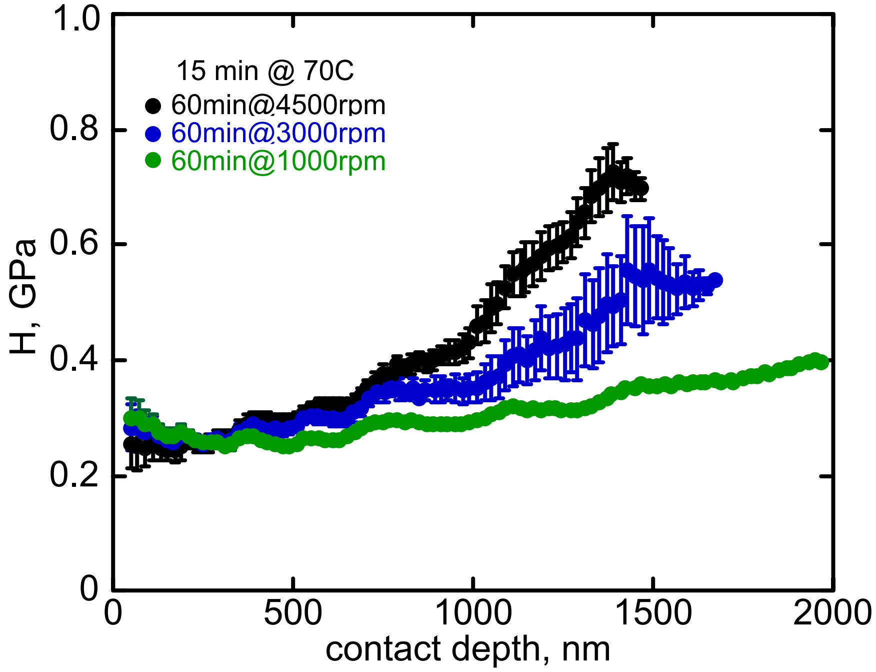

(b)

Figure 2.7. Modulus (a) and hardness (b) as a function of contact depth for samples precured for 15 minutes at 70°C.

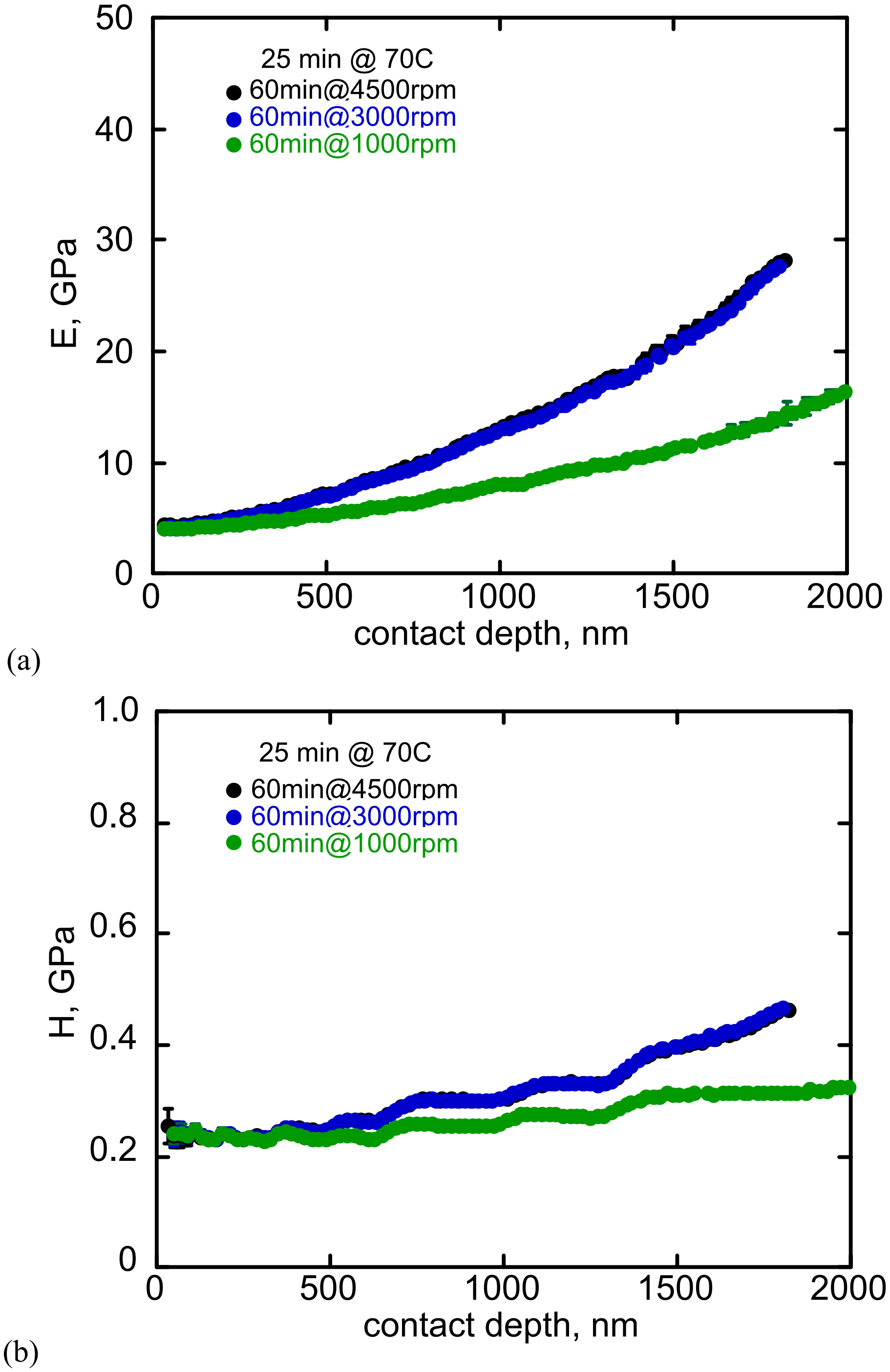

Figure 2.8. Modulus (a) and hardness (b) as a function of contact depth for samples precured for 25 minutes at 70°C.

The effect of precure time and spin speed of the neat films' modulus and hardness was further investigated using the near-surface modulus and hardness values. Modulus and hardness are presented as a function of precure time in Figure 2.9. Both modulus and hardness decrease as a function of precure time. For the shorter precure times, a spin-rate effect is observed; higher spin rates lead to larger modulus and hardness values.

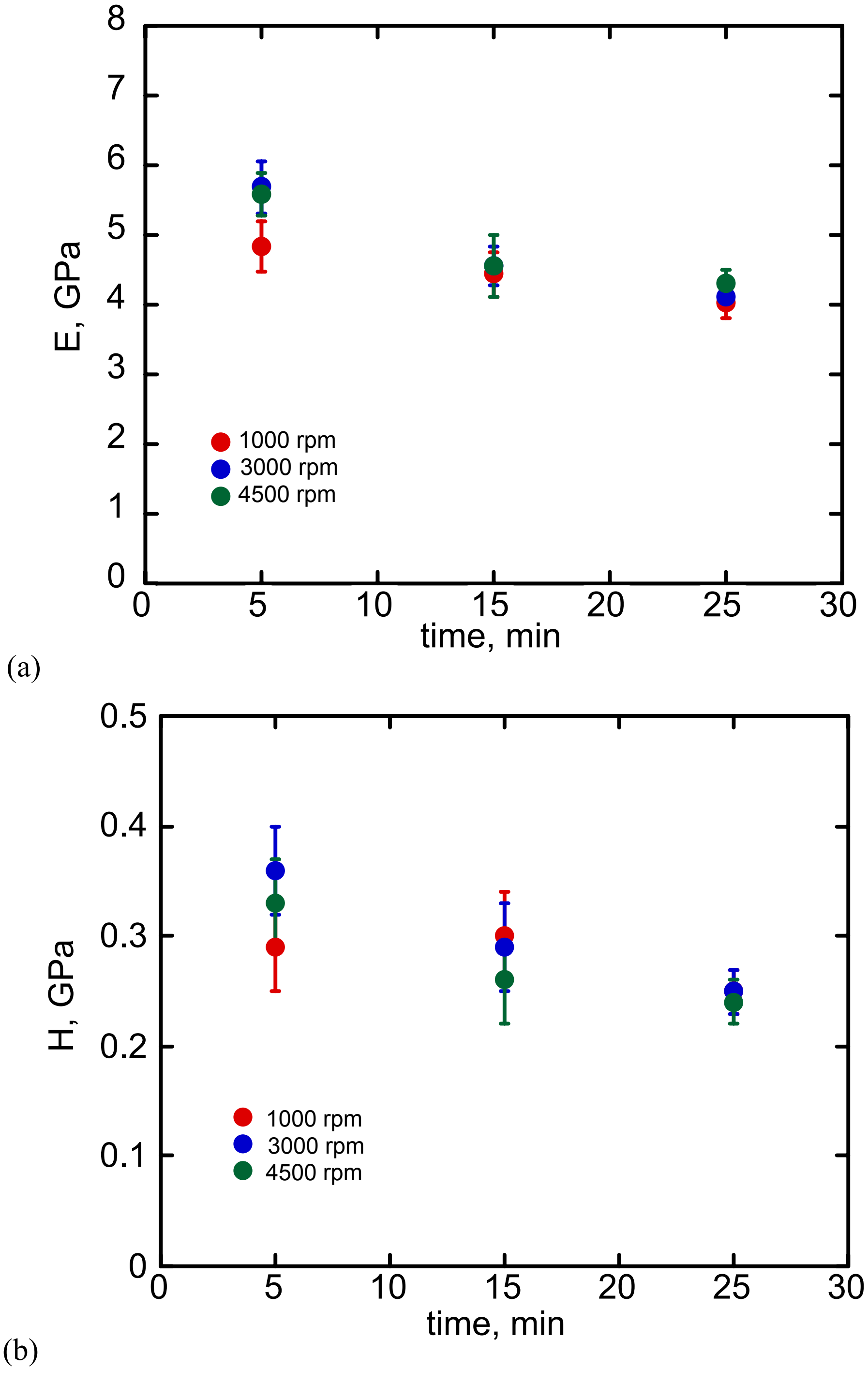

Figure 2.9. Near-surface modulus (a) and hardness (b) as a function of precure time for three spin rates.

To understand this effect, the same data are plotted as a function of spin rate in Figure 2.10. No difference in modulus or hardness is observed as a function of spin rate.

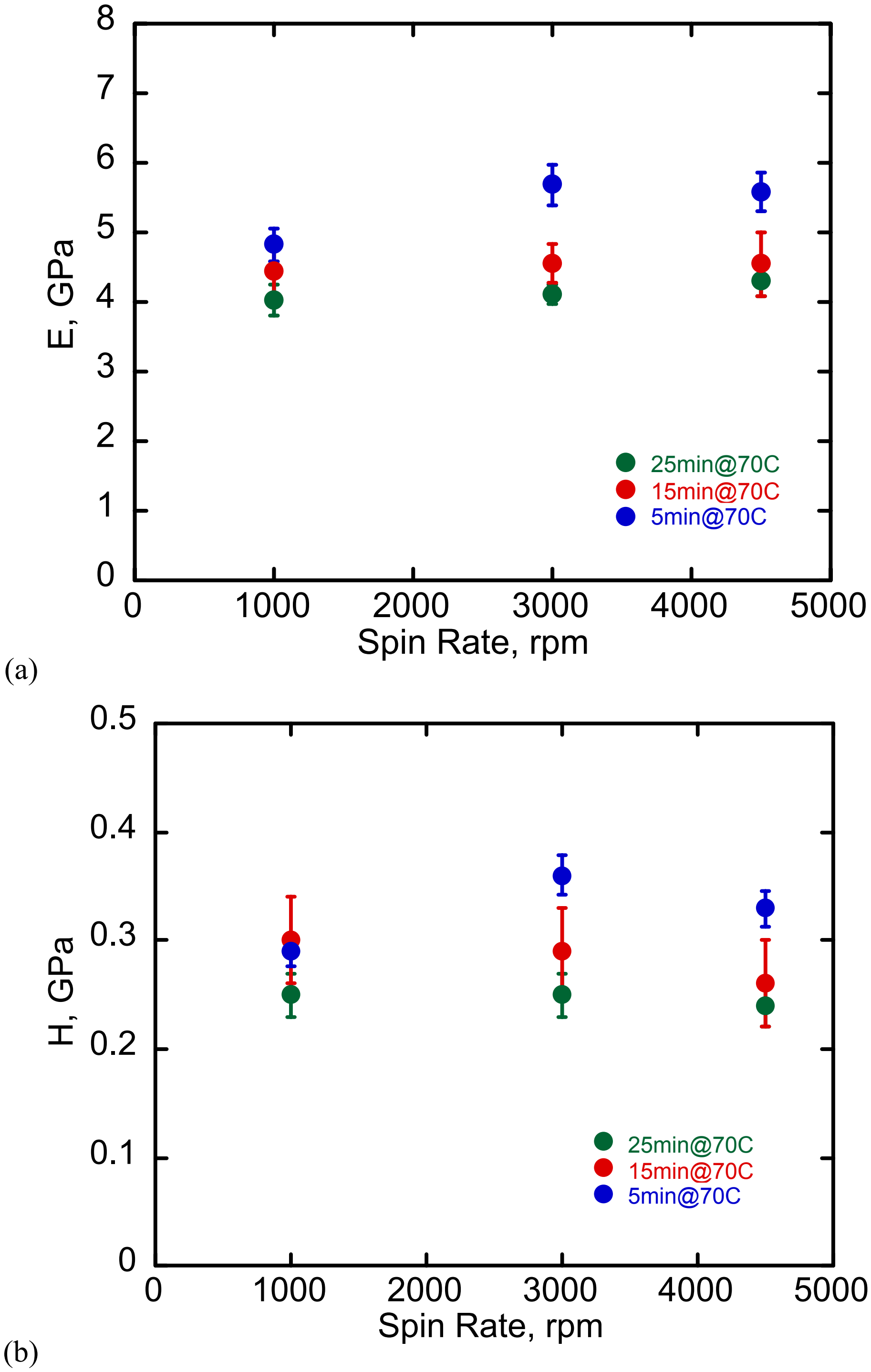

Figure 2.10. Near-surface modulus (a) and hardness (b) as a function of spin rate for three precure times.

We would expect that the spin rate and precure time would both have an effect on the film thickness. To determine if the increased modulus observed in the sampled precured for 5 minutes is related to the film thickness, we examined the film thickness as a function of spin rate for the different precure times. This data is presented in Figure 2.11.

For all precure times, thinner films are achieved with faster spin rates, as expected. We would also expect that thinner films would be formed when shorter precure times were used, since the viscosity increases as the cure reaction takes place. This trend is not observed, however. The thickest films are formed from the 25 minute precure, as expected, but the 5-minute precure led to films that were thicker than the 15-minute precure. We hypothesize that this result is due to thermal lag while heating the epoxy. A sample in a 70°C oven for five minutes is not likely to be in thermal equilibrium, and thus would have a viscosity closer to the room temperature viscosity when applied to the substrate. It appears that the sample precured for 15 minutes reached a minimum viscosity, where it is in thermal equilibrium but little or no cure has taken place.

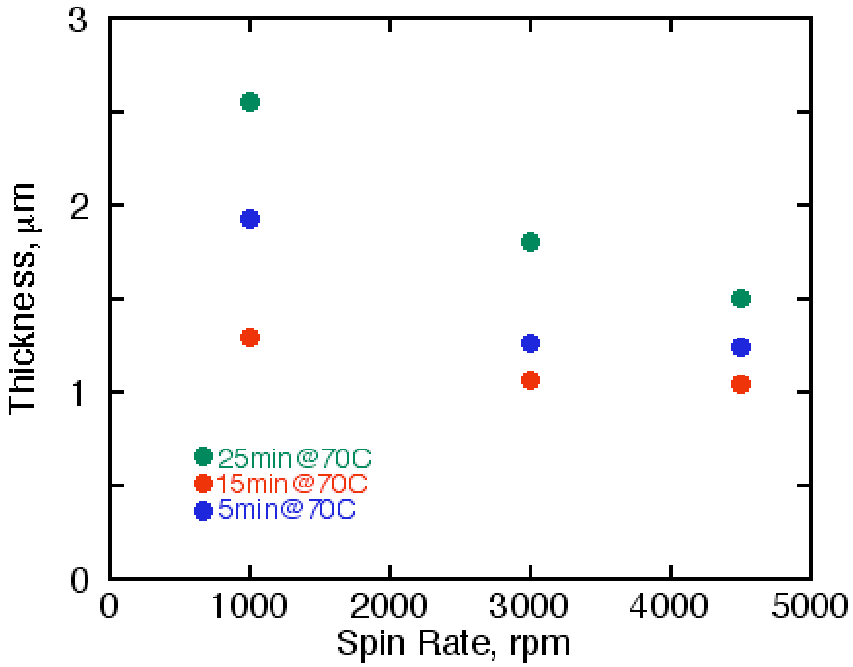

Figure 2.11. Epoxy film thickness as a function of spin rate for three precure times.

In Figure 2.12, the epoxy film modulus and hardness are presented as a function of film thickness. In the modulus vs. thickness plot, a slight trend of decreasing modulus with increasing film thickness is observed. For the samples precured for 5 minutes, however, the modulus is consistently higher than for other samples of comparable thickness. A similar trend is observed in the hardness vs. thickness plot, however, the trend is less well defined due to increased scatter in the data. A likely explanation for the difference in modulus based on precure time is that a different cure mechanism is achieved during the precure and the final cure. Two important differences exist during the precure and the final cure. First, the precure takes place at a higher temperature than the final cure, 70°C vs. 50°C. Second, the final cure takes place in a thin film form in which mobility may be restricted. A third possible contribution to the differences observed is that the final cure takes place with the epoxy adjacent to aluminum oxide, which could catalyze a different reaction mechanism. If mechanism A, the cure mechanism during the precure, leads to a lower crosslink density than mechanism B, the dominant mechanism during the final cure, then samples precured for a shorter period of time would have a lower modulus.

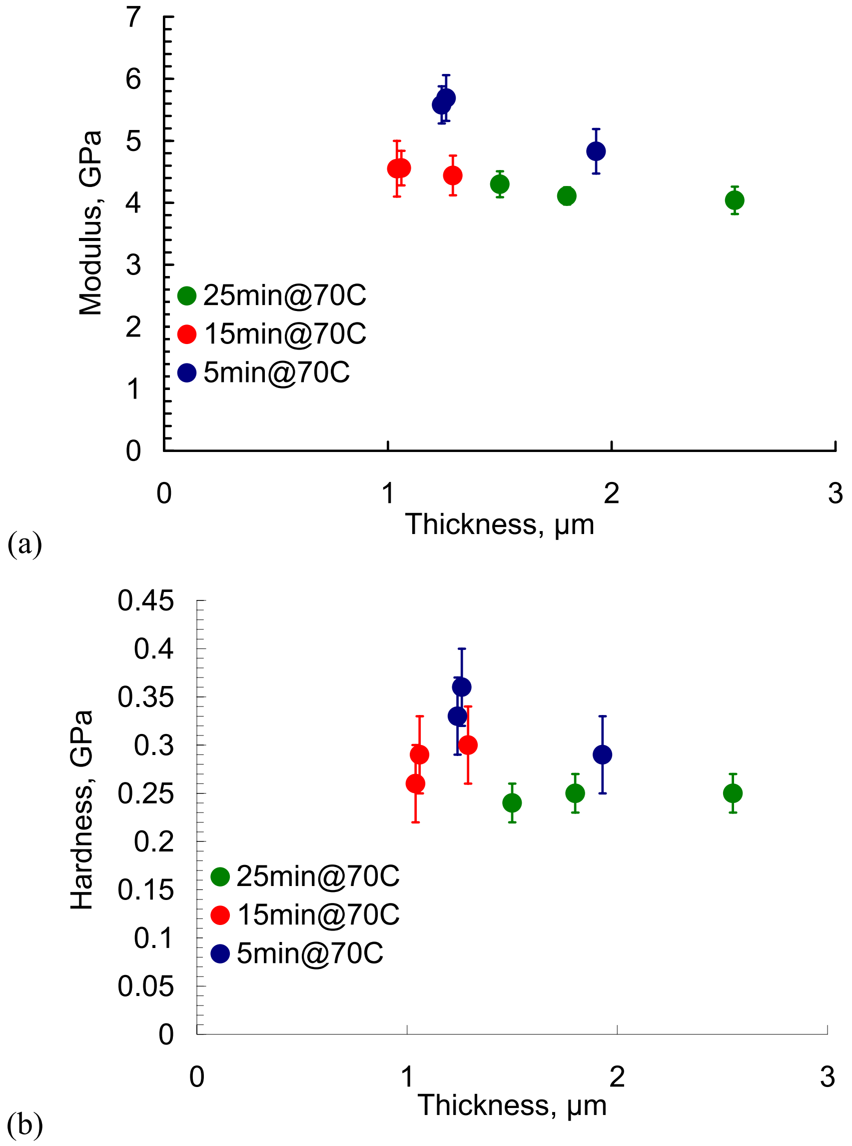

Figure 2.12. Modulus (a) and hardness (b) as a function of epoxy film thickness for three precure times.

Yield strength was then estimated for all films using the empirical relationship between hardness and yield strength of glasses and glassy polymers (Figure 2.13) derived by Marsh.[18] This is a complex relationship depending on elastic properties as follows,

$$H/\sigma_{ys} = C + KB\ln(Z) \qquad \textbf{Equation 2.1}$$

In this expression

$$\lambda = (1\text{-}2\nu)/\sigma_{ys}/E \qquad \textbf{Equation 2.2}$$

$$\mu = (1+\nu)\sigma_{ys}/E \qquad \textbf{Equation 2.3}$$

$$B = 3/(3 - \lambda)$$ **Equation 2.4**

$$Z = 3/(\lambda + 3\mu - \lambda\mu)$$ **Equation 2.5**

Where σ_{ys} is the yield strength, C and K are constants, H is hardness, E is elastic modulus, and ν is poisson's ratio.

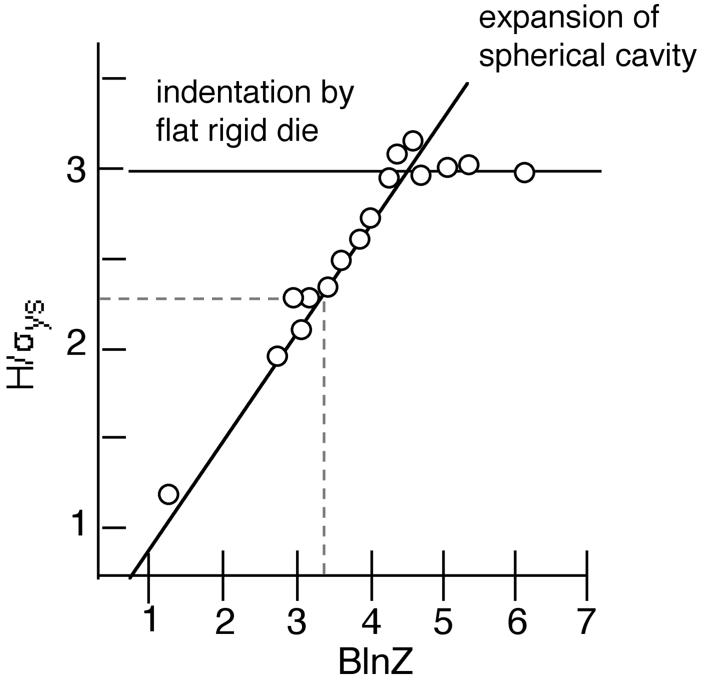

Figure 2.13. The relationship derived by Marsh (1963) shows a linear relationship exists between yield strength and properties for glasses and glassy polymers.

Using C=0.28, and K=0.6, measured elastic moduli and hardness values, and ν = 0.38, the yield strengths for all films were determined. These values are given in Table 2.2. With the exception of the 5 minute cured films, the measured elastic moduli and hardness values compare well with the spun cast elastic modulus of 4.35 GPa, hardness of 250 MPa, and yield strength of 115 MPa.[20] These values are slightly higher than the elastic modulus of 3.5 GPa and yield strength of 90 MPa measured using compression tests on bulk samples.[7]

One interesting relationship to note is that the yield strengths do not follow hardness but scale with film thickness. This is the same behavior, though much less pronounced, exhibited by thin ductile metal films where strength increases markedly as film thickness decreases. In metals films, this increase results from a marked increase in the resistance to dislocation motion. It is unclear as to what process would increase resistance to deformation in thin polymer films or if the increase is due to test technique creating a pressure effect on measured values.

Following characterization of the melt spun films on aluminized glass substrates, thin epoxy films were melt spun onto as-machined 60612-T6 aluminum substrates. Each system received a unique combination of FLP etch, plasma clean, and primer coat. Ten indents were run on each sample from which properties were determined as a function of contact depth. These data are shown in Figure 2.14. These were relatively thick samples, with no apparent effect of substrate properties was observed. There was significant statistical scatter in the near surface hardness values which may be the result of the very sensitive nature in defining the point of initial surface contact. As a consequence, properties were determined in the plateau region just beyond the surface. These data are given in Table 2.4. They are lower than corresponding values measured in the thinner melt spun on aluminized glass films but essentially the same as values measured by bulk sample compression testing.

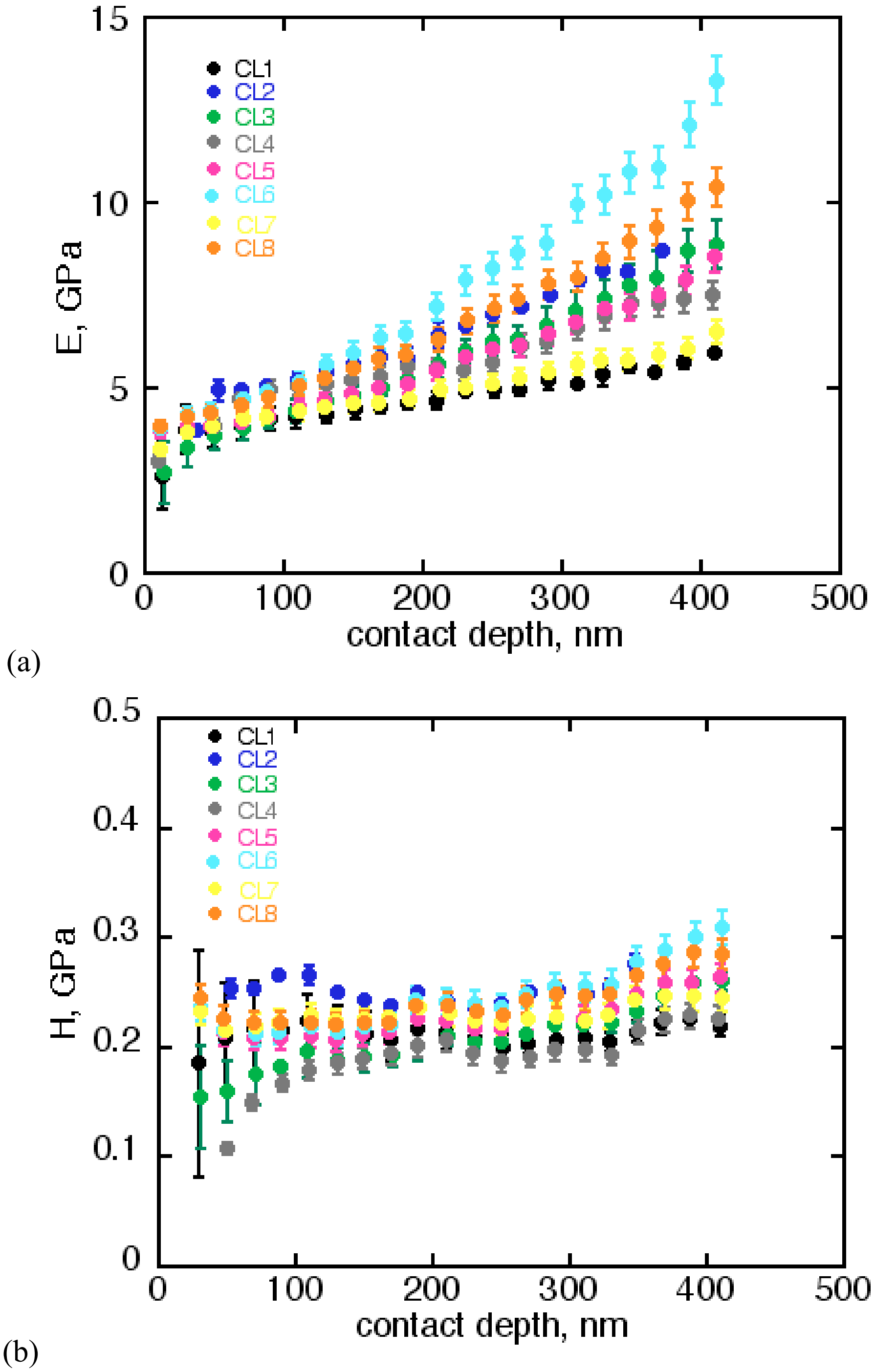

Figure 2.14. Modulus (a) and hardness (b) as a function of contact depth for samples with different processing steps performed.

Table 2.4. The effect of process techniques on properties of melt spun Epon 828/T403.

Sample	*E*, GPa	*H*, GPa	Yield Strength, MPa
CL1	3.61±0.26	0.21±0.017	93
CL2	4.46±0.19	0.25±0.015	110
CL3	3.19±0.30	0.20±0.012	91
CL4	3.92±0.66	0.19±0.023	79
CL5	3.47±0.28	0.22±0.01	101
CL6	3.55±0.47	0.23±0.010	100
CL7	3.78±0.23	0.23±0.012	98
CL8	3.74±0.29	0.23±0.01	98

2.3.2. Thin Film Delamination

Energies sufficient to trigger delamination could not be generated by indentation in the thin films of this study. This necessitated deposition of highly stressed overlayers to trigger delamination. Following the work of Bagchi and Evans,[10] Bagchi et al.,[9] Kriese and coworkers[11,12] and Zhuk et al.,[13] highly stressed overlayers of tungsten were deposited onto the thin films. The deposition process was developed for this study and a study on spun cast epoxy films by David Adams, 14171, and Prof. David Bahr at Washington State University.[21] The technique was then used to deposit stressed overlayers on all films melt spun on aluminized glass substrates. The deposition triggered extensive areas of wrinkle formation across most sample surfaces and telephone cord blisters in several more. (Figure 2.15) In contrast with companion work on spun cast films, there was no evidence of interfacial failure along the film substrate interfaces. When blisters formed, they formed along the overlayer-epoxy film interface.

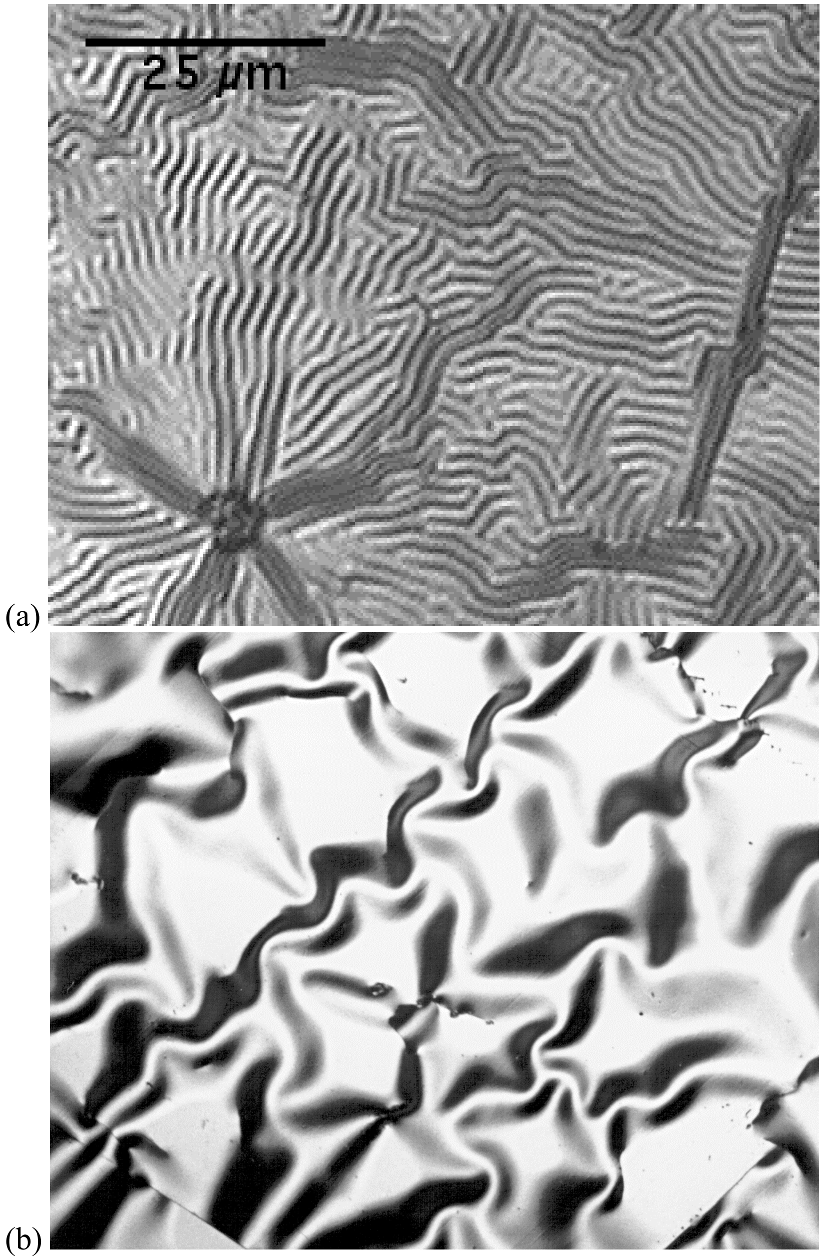

Figure 2.15. (a) Wrinkles and (b) telephone cord blisters that formed when stressed overlayers were deposited on the melt spun films.

2.3.3. Fracture Energy Analysis

2.3.3.1. Thin Film Telephone Cord Blister Formation

Interfacial fracture energies were obtained for films that exhibited telephone cord blistering using solutions for film systems where residual stresses drive fracture. These solutions were originally derived for single layer film-on-substrate systems[2,22,23]. Work by Bagchi et al.,[9] Bagchi and Evans,[10] and more recently by Kriese et al.[11,12] extended these solutions to multilayer systems by treating the multilayer film as a single film of the same total thickness with a transformed moment of inertia. For failure along the overlayer-epoxy film interfaces in this study, the single layer solutions were used to determine interfacial fracture energies. The blisters are modeled as wide, clamped Euler columns of width *2b*. For a blister to form between the overlayer and epoxy film, the compressive residual stress, σ_r, must exceed the stress for interfacial delamination, σ_b, as follows,[2]

$$\sigma_b = \frac{\pi^2}{12}\left[\frac{E_{ep}}{\left(1-\nu_{ep}^2\right)}\right]\left(\frac{h}{b}\right)^2 \qquad \textbf{Equation 2.6}$$

In this expression, ν_{ep}, is Poisson's ratio for the epoxy film, *b* is the blister half-width, and *h* is the tungsten overlayer thickness.

The residual stress can then be determined from the blister height and the stress for delamination as follows,[2]

$$\sigma_r = \sigma_b\left(\frac{3\delta^2}{4h^2}+1\right) \qquad \textbf{Equation 2.7}$$

where δ is the buckle height and σ_b is given by Equation 2.6.

Optical profilometry and AFM were used to measure blister heights and widths. Measurement location and schematic blister profile are shown in Figure 2.16. Combining these measurements with the elastic modulus and Poisson's ratio for Epon 828/T403, a compressive residual stress of -2.1 GPa was calculated for the tungsten overlayers on the epoxy films. This value is in good agreement with compressive stress measurements of -2.2 GPa from tungsten on glass samples run under identical deposition conditions in the same sputter chamber. This agreement supports the application of these mechanics-based, elastic isotropic solid models for estimating interfacial fracture energies in this thin epoxy film system.

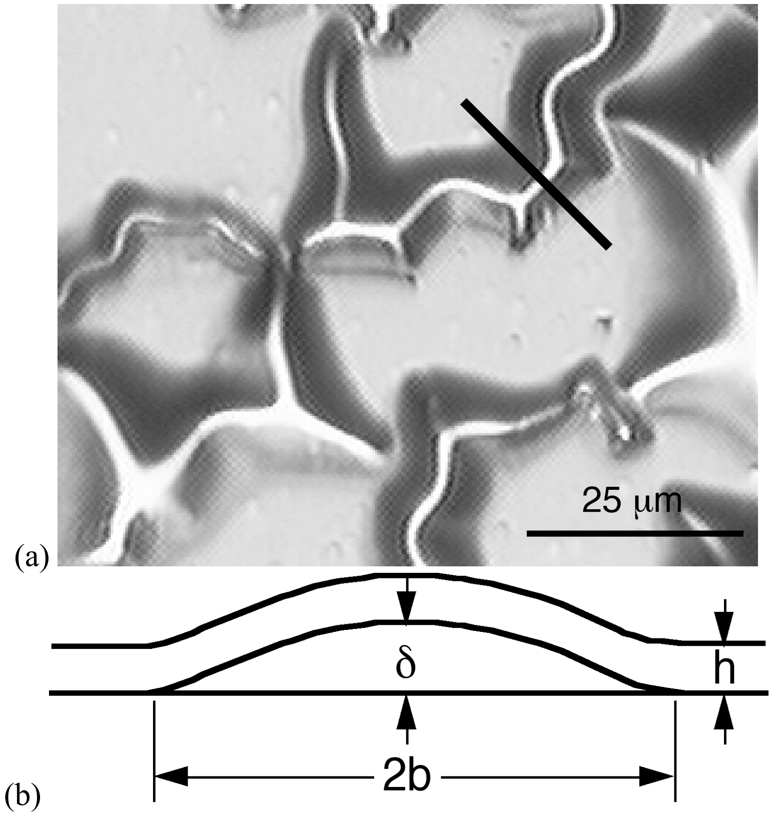

Figure 2.16. (a) Measurement location and (b) schematic of a telephone cord blister profile.

The residual stress and stress for delamination were then used to determine the strain energy release rate for interfacial fracture along the straight side wall portions of the telephone cord blisters from,

$$\Gamma(\Psi)=\left[\frac{\left(1-\nu_{ep}^{2}\right)h}{2E_{ep}}\right](\sigma_r-\sigma_b)(\sigma_r+3\sigma_b)$$ **Equation 2.8**

The measured fracture energies are given in Table 2.5. These results show that fracture energies approach a lower limiting value.

Table 2.5. Average film thickness, heights and blister half-widths, delamination stresses, residual stresses, and fracture energies from telephone cord blisters in melt spun Epon 828/T403 films.

	Thickness		Blister		Stress		Fracture Energy			
Sample	h_{ep} (nm)	h_W (nm)	δ (μm)	b (μm)	σ_b (MPa)	σ_r (GPa)	G_o* (J/m^2)	$\Gamma(\psi)$ (J/m^2)	ψ	Γ_I (J/m^2)
MS3	2550	450	2.58	22.7	150	-3.7	6.2	7.9±2.6	-74	3.0±1.0
MS7	1040	450	2.43	25.2	120	-2.7	6.2	4.1±1.6	-76	1.5±0.7
MS8	1060	450	2.40	24.3	110	-2.9	6.2	4.6±1.0	-74	1.8±0.5

2.3.3.2. Mode I Fracture Energies

Interfacial fracture is often treated as a mode I failure with mode I energies at crack arrest set equal to the practical work of adhesion.[2] The measured fracture energies are comprised of mode I normal and mode II shear contributions and varies with blister morphology (Figure 2.17). Several criteria have been proposed to characterize contributions based on the phase angle of loading, ψ. This angle is defined as the tangent of the ratio between shear and normal forces at the crack tip. Of these criteria, the following relationship is often found to realistically reproduce data for interfacial fracture,[2]

$$\Gamma_I = \frac{\Gamma(\Psi)}{\left\{1+\tan^2\left[(1-\lambda)\Psi\right]\right\}} \qquad \textbf{Equation 2.9}$$

where λ is a material parameter equal to 0.3 for most materials. It should be noted that significant reservations have been raised concerning determination of the phase angle for multilayer systems,[12] especially when crack growth is accompanied by significant plastic deformation.[8,24,25] Relatively low measured fracture energies and thin films suggest that plastic deformation is not a significant factor in interfacial fracture for the films of this study. The phase angle of loading was then estimated using the following equation for telephone cord and circular blister formation as follows,[2]

$$\Psi = \tan^{-1}\left[\frac{\left(\cos\omega + \frac{h\Delta N}{\sqrt{12}M}\sin\omega\right)}{\left(-\sin\omega + \frac{h\Delta N}{\sqrt{12}M}\cos\omega\right)}\right] \qquad \textbf{Equation 2.10}$$

In this equation, ΔN is the in-plane stress, M is the bending moment, and ω is a dimensionless function describing the elastic mismatch between the film and the substrate. The value for $h\Delta N/(\sqrt{12}\,M)$ is determined from numerical solutions based on an effective driving force of σ_r/σ_b for telephone cord blisters.[2] ω is set equal to -53.1° to account for the effect of elastic mismatch between the tungsten overlayer and epoxy.[26] With these values, the phase angles of loading for blisters were determined using Equation 2.10.

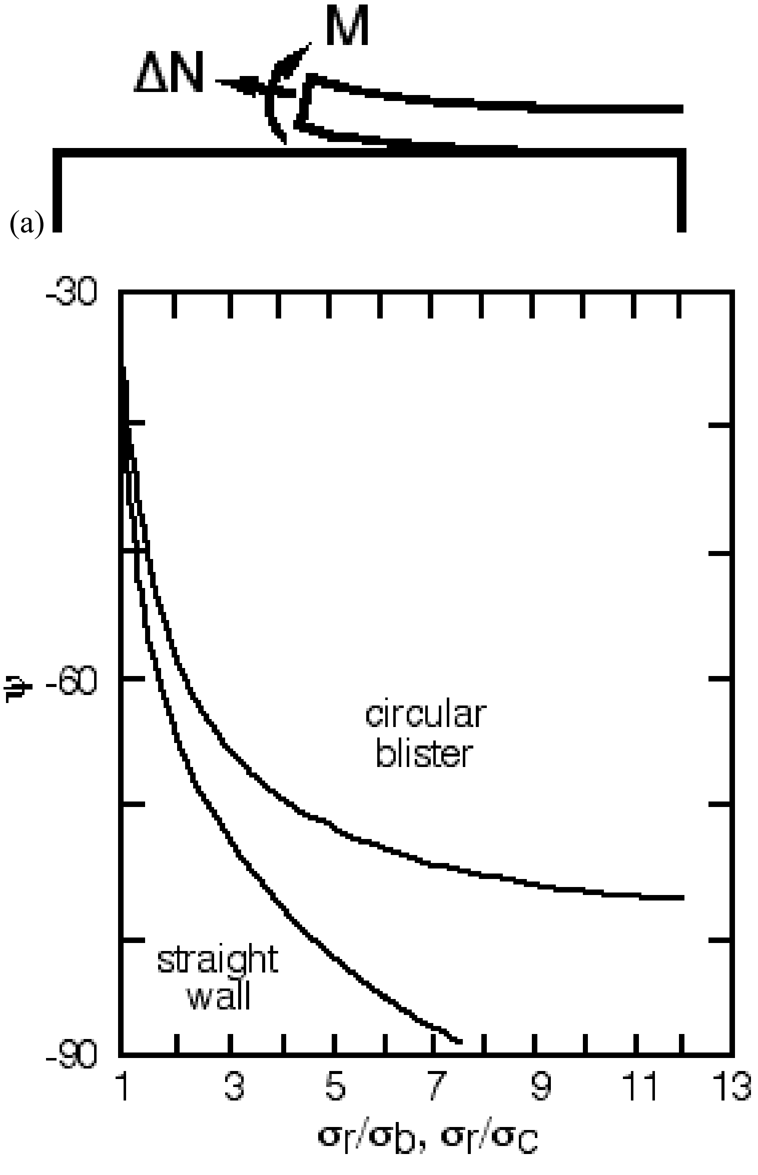

Figure 2.17. (a) Schematic of blister cross-section showing moments and loads from which (b) phase angles of loading for circular and telephone cord (straightwall) blisters were calculated as a function of effective driving force. From Hutchinson and Suo (1992).

Mode I fracture energies were determined using Equation 2.8 through Equation 2.10 and are given in Table 2.5. These values are significantly higher than the true work of adhesion for uncured epoxy oliogomers on a methyl-terminated aluminum surface of 50 mJ/m^2.[7] They are also higher than the mode I fracture energy near 0.5 J/m^2 observed in spin cast films. However, the higher fracture toughness values may be due to an increased capacity for plastic energy dissipation in thick films. We therefore compared the melt spun with spin cast film fractures on the basis of total stored energy. Figure 2.18 shows that the total stored energy in the melt spun films is greater than the stored energy in the spin cast films. Moreover, it is more than sufficient to drive blister formation in the spin cast films. These results suggest that melt spinning creates a stronger interface bond between the film and substrate than the spin cast process.

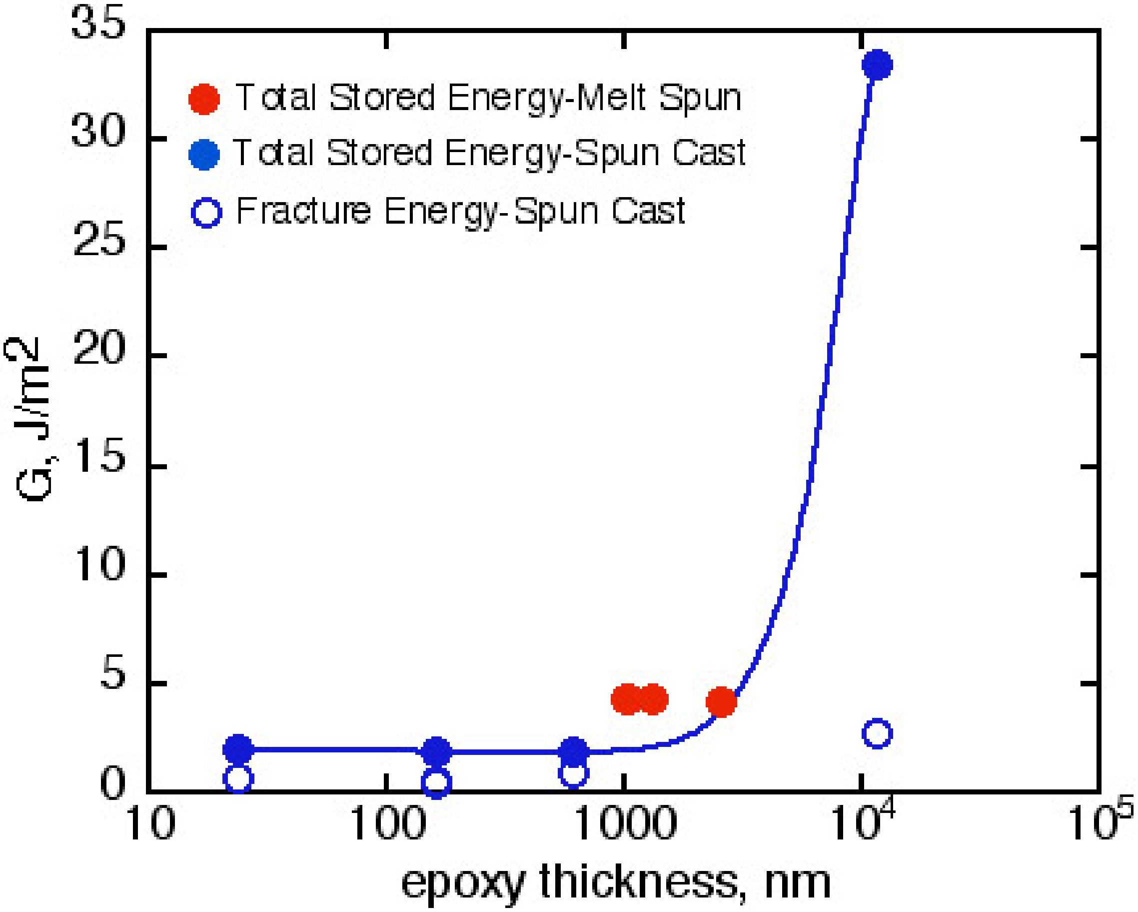

Figure 2.18. The total stored energy in melt spun films is greater than the total stored energy that triggered interfacial fracture in spin cast films.

3. Contact Mechanics

3.1. Background

Surface contamination is a widespread problem in the adhesive bonding of micro-assemblies, and therefore calls for a convenient method to assess the cleanliness of the adherends before introducing the adhesive to the microsystem. Surface cleaning or preparation by means of solvents is the most common process step in many electronic manufacturing operations.[27] In qualifying a new solvent, the engineer must rely on cumbersome laboratory tests, which are costly, repetitious, and time-consuming. In metal machining, the lubricants employed in the process must be removed; however, many of the cleaning solvents that were once used are now banned because of health hazard and ozone depletion regulations. Overcleaning is a concern, as it increases the waste stream, as well as the cycle time of the product, resulting in increased product cost.[27] Therefore, understanding the link between surface preparation and adhesion can lead to a reduction in the time required for development and testing of cleaning procedures. It can also lead to improved bondlines and enhanced manufacturability, enabling product realization for encapsulated components.

Molecular modeling has been employed to elucidate the behavior of a low molecular weight contaminant near an interface between a polymer adhesive and a substrate.[27-30]

Depending on the substrate-polymer and polymer-polymer interactions, as well as the molecular architecture of the contaminant and polymer, the contaminant can preferentially diffuse toward the interface.[27,31] When this happens, the contaminant molecules will displace the polymer from the interface, as illustrated in Figure 3.1, resulting in a degradation of the adhesive bond strength.[27] A modeling effort has also been undertaken by Shanahan[32] to examine the role of diffusion in the wetting of a contaminated surface. Results of modeling indicate that a thin layer of a second liquid present on the substrate (the contaminant) can penetrate the sessile drop of liquid deposited on the solid surface and gradually change the effective interfacial free energy between the substrate and the drop.[32]

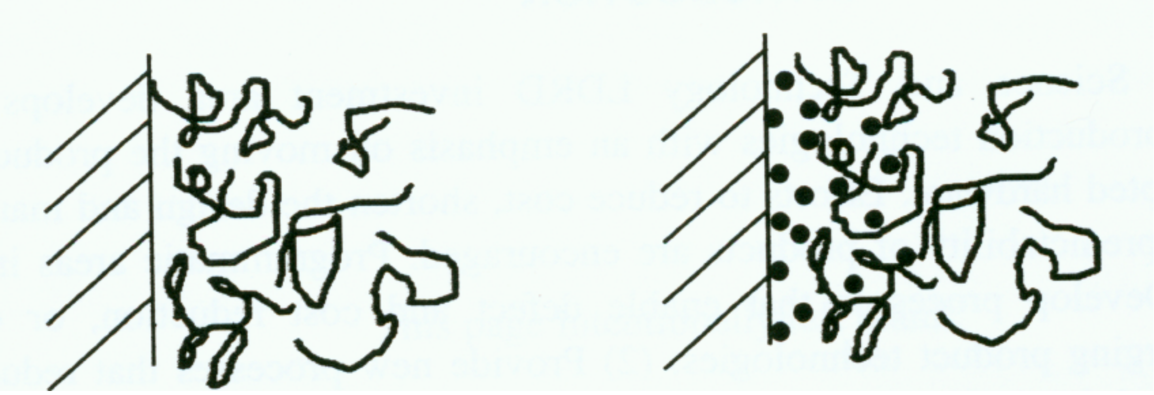

Figure 3.1. Schematic of a polymer adhesive/substrate interface in the absence (left) and presence (right) of surface contamination. In the latter case, the contaminant molecules can displace the polymer from the interface resulting in a degradation of the adhesive bond strength. Adapted from [27].

3.1.1. Overview of Present Work

Surface analysis techniques, including X-ray photoelectron spectroscopy, Auger spectroscopy, and secondary ion mass spectroscopy, are routinely employed to characterize surface properties of substrates, however these ultra-high vacuum techniques are obviously impractical for probing liquid contaminants. The JKR[33] contact mechanics technique, on the other hand, has a number of unique advantages for examining micron-scale areas in a processing environment, as it is relatively inexpensive, versatile, easy to operate, and can be operated in ambient conditions. In recent years, a number of researchers in the adhesion community[34-47] have employed the JKR technique to analyze the fundamental forces of adhesion between two materials. A particularly noteworthy advantage of the contact mechanics experiment is the very low crack growth speeds which are accessible with this technique, affording us higher sensitivity as compared with other adhesion tests such as the peel test.[34-47]

In the present work, we use the JKR method as a means to assess the level of contamination at an epoxy/aluminum oxide interface. This was achieved by conducting JKR experiments in the presence and absence of an organic contaminant. The model contaminant is hexadecane, a non-polar hydrocarbon fluid of medium molecular weight. We chose hexadecane because it replicates typical machining fluids, is non-reactive with aluminum oxide surfaces, and should not readily dissolve into the adhesive system of interest.

3.1.2. Overview of JKR Contact Mechanics

The JKR theory, developed by Johnson, Kendall, and Roberts[33] is an extension of the Hertz analysis,[34, 48] which relies on a fracture mechanics-energy balance approach to describe the mechanics of interaction in the presence of adhesive forces. A salient feature of the JKR contact mechanics approach is that it allows one to make a direct estimate of the work of adhesion, *W*, between the two solids of interest, unlike the conventional contact angle experiment, which requires the user to construct a calibration curve. Chaudury and Whitesides[34] led the renewed interest in the JKR contact mechanics technique, having developed an experiment based on the use of soft, hemispherical lenses on rigid, flat plates. In this technique, a material of low elastic modulus, in the shape of a hemispherical lens is brought into contact with a solid surface of interest, and the resultant contact area is monitored as a function of applied loading and lens penetration depth. The contact area varies with applied loading according to the JKR equation (Equation 3.1), which describes the system behavior as a function of its geometry, material properties, and adhesive forces:

$$a^3 = \frac{R}{K}\left\{P + 3\pi WR + \left(6\pi WRP + (3\pi WR)^2\right)^{\frac{1}{2}}\right\}$$

Equation 3.1

where a is the contact radius, R is the effective radius of the system, K is the effective bulk modulus of the material, P is the contact load, and W is the work of adhesion. The JKR predictions give rise to a second relationship, which describes the lens penetration depth, δ, as a function of P, a, R, and K

$$\delta = \frac{a^2}{3R} + \frac{2P}{3aK}$$

Equation 3.2

Researchers have previously demonstrated[39, 41, 44] that use of these two equations simultaneously provides an internal check of the validity of the small deformation approximation used in the JKR analysis. In particular, JKR theory assumes small deformations so that the depth of the strain field at the elastomer-rigid support interface is negligible compared with the depth of penetration.[44] Therefore, when the JKR contact mechanics technique is used to measure the work of adhesion between two solids in contact, it is now an adopted custom to analyze the plot of δ vs. a to assess whether or not the experimental data deviate from the JKR prediction at large contact areas.[39, 41, 44, 45] Deruelle et al.[44] have demonstrated that one can circumvent this problem by intercalating a thick ribbon of the same elastomer between the lens and its support. Alternatively, the experimentalist can make a special point of not over-compressing the elastomeric hemisphere during the loading experiment,[41, 45] or in other words, can avoid deforming the hemisphere laterally, which has been known to occur if measurements are made at exceedingly large contact areas.[41]

Presented below is a schematic of the JKR experiment (Figure 3.2), as well as sample data obtained during a JKR compression experiment (Figure 3.3).[45] In all cases, the symbols represent the data points and the solid lines trace the fits to the data for an epoxy lens against a γ-amino-propyl-triethoxysilane-modified silicon substrate. Figure 3.3(a) depicts the contact radius cubed versus applied load (a^3 vs. P), while Figure 3.3 (b) and (c) illustrate the relationships between δ and a, and δ and P, respectively. In this particular case, the suitability of the JKR model was excellent, which suggested that the experiment had been performed within the constraints of the theory. In general, it is advisable to perform such calibration experiments to check the performance of the epoxy lens against a variety of substrates.

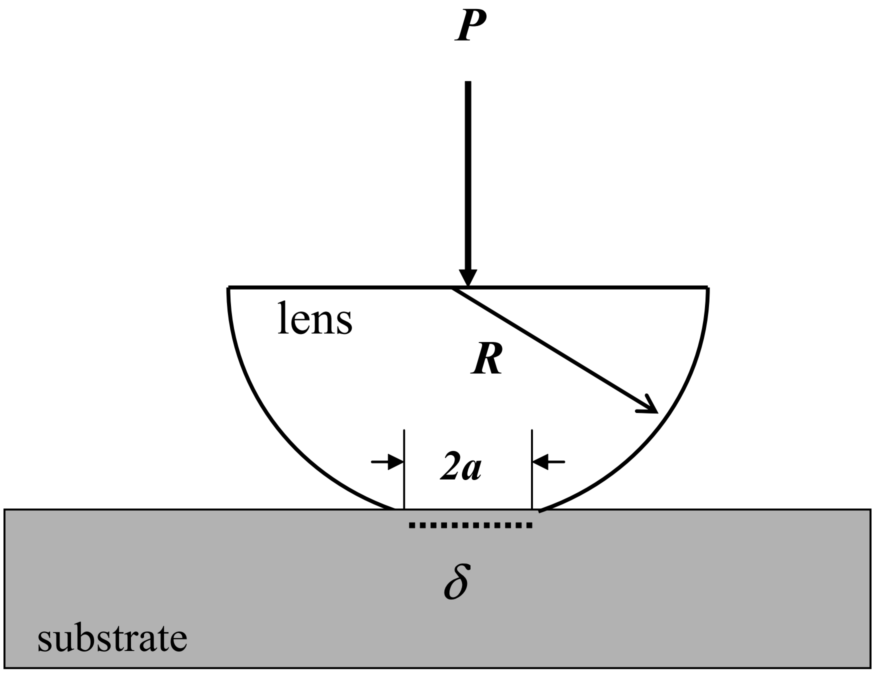

Figure 3.2. Schematic illustration of the JKR contact mechanics experiment, where *P* is the load, *a* is the lens contact radius, *δ* is the penetration depth of the lens, and *R* is the radius of curvature of the lens.

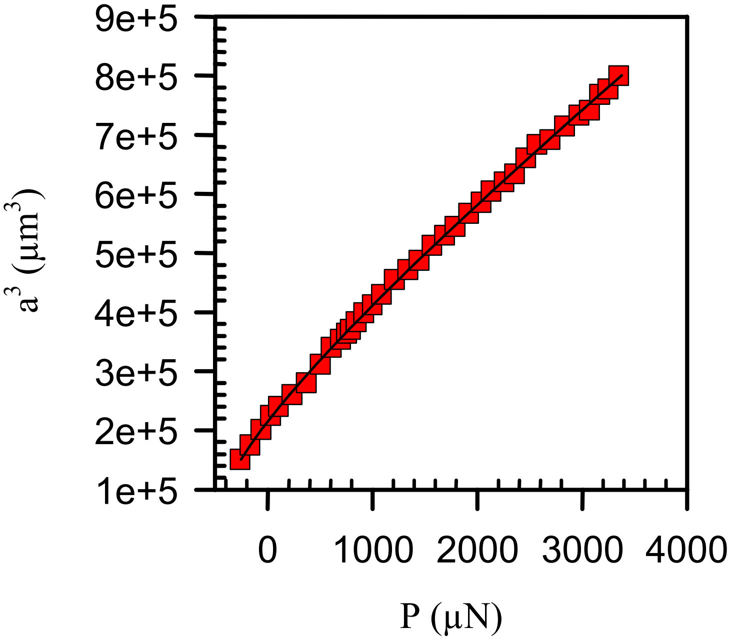

(a)

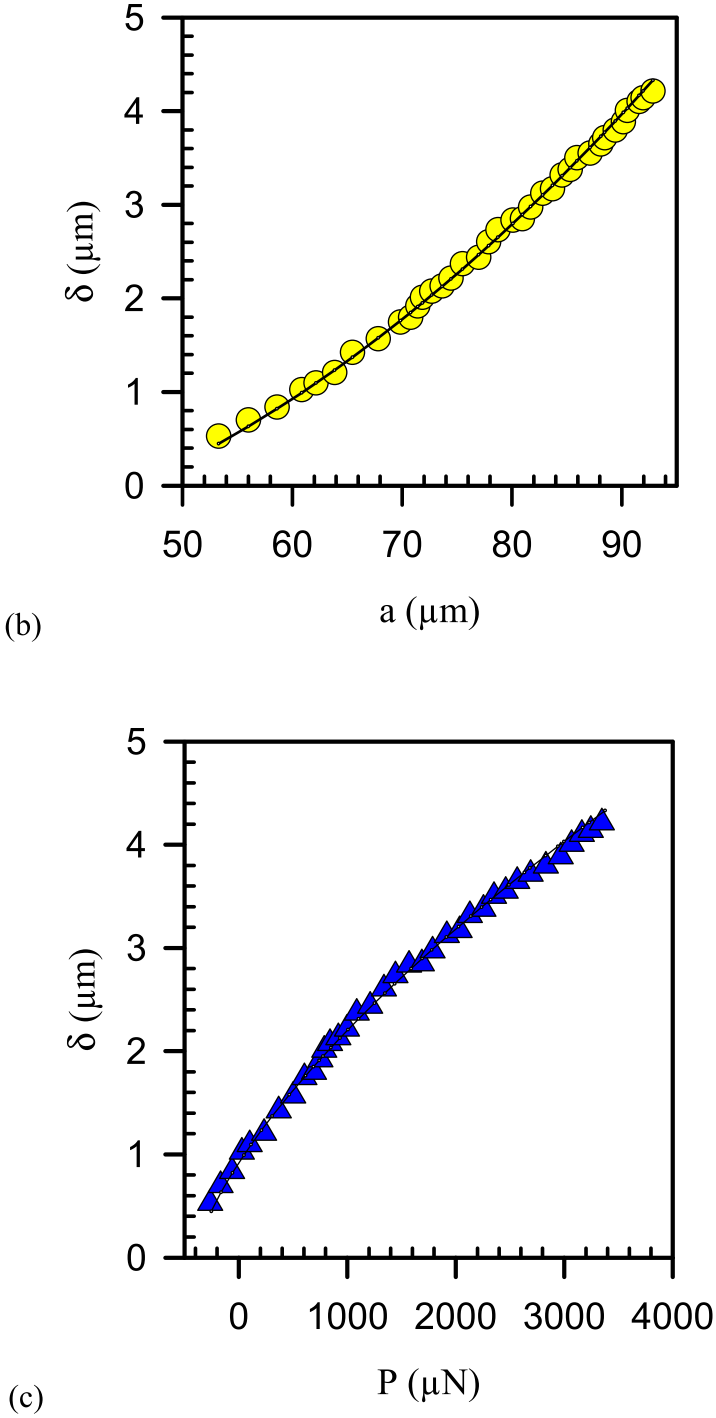

Figure 3.3. Typical curves obtained from a single JKR loading experiment. In all cases, the symbols represent the data points and the solid lines trace the fits to the data for an epoxy lens against a γ-aminopropylsilane-modified silicon wafer. (a) Contact radius cubed vs. applied load; (b) displacement vs. contact radius; (c) displacement vs. applied load. Adapted from [45].

3.2. Materials and Procedures

3.2.1. Contact Mechanics Experiment

A schematic of the JKR apparatus is depicted in Figure 3.4. A Questar QM100 Lens optical microscope equipped with a CCD camera is used to observe the contact area through the transparent elastomer lens. Images are captured by a video camera and imported directly into a computer image analysis program (Image Pro Plus). In each of the experiments, the elastomeric lens is mounted directly to the bottom of a glass microscope coverslip, which is attached to the upper arm of the precision stage (Figure 3.4).

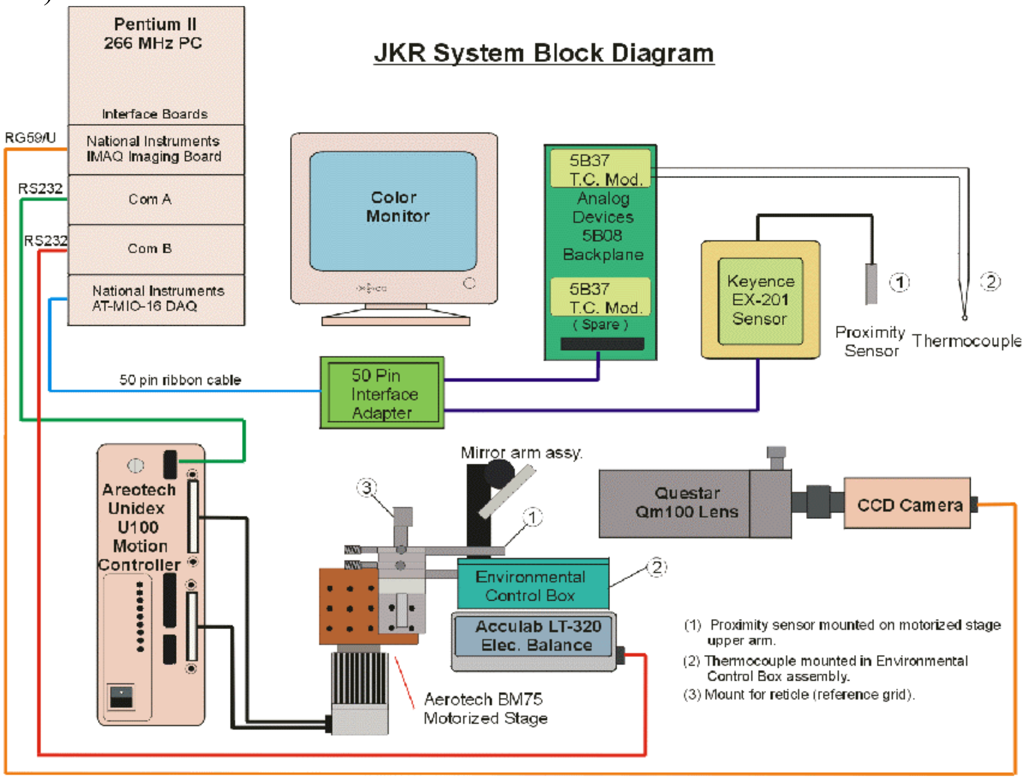

Figure 3.4. Block diagram of JKR system used for contact mechanics studies.

Quasi-equilibrium loading experiments$^{39\text{-}41, 44, 45}$ were performed by imposing 1-µm compressions every five minutes, allowing the system to relax before acquiring real-time measurements of the contact area, load, and displacement. The maximum load is selected by the experimenter, and may vary from one run to the next. The contact radii were determined with the ImagePro Plus software of ± 1 µm accuracy, and compression was measured with a proximity sensor (Keyence, EX-305) mounted on the upper arm of the motorized stage. Unloading experiments were conducted by reversing the motor, and once again, capturing the data over time until the surfaces were completely separated. In this experiment, the vertical displacements of 1 µm correspond directly to the compression of the lens. (The height of the balance is controlled with a linear variable displacement transducer, and is automatically returned to its original position after each displacement.) All measurements were made at room temperature and at 30-60% RH.

3.2.2. Preparation of Epoxy Elastomers

Elastomeric probes were prepared by mixing stoichiometric quantities of diglycidyl ether of bisphenol A (DGEBA) epoxy resin (Dow Chemical, DER 332, MW=356 g/mol, or DER 331, MW = 365-384 g/mol) with one of two polyoxyalkyleneamine curing agents, Jeffamine ED-900 and ED-2003 (Hunstman Chemical, MW = 900 or 2003), to produce both "high" modulus and "low" modulus *elastomeric* lenses (Figure 3.5). Each mixture was stirred for several minutes at room temperature and subsequently degassed. The elastomeric hemispheres were formed by applying small drops of the reactive mixture onto fluorinated glass plates, which were later cured at 120°C for roughly 20 hours.

Diglycidyl ether of bisphenol A MW = 340 g/mol

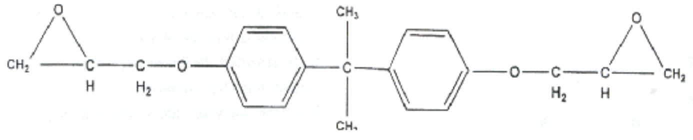

DER 331 Avg. MW = 365-384 g/mol DER 332 Avg. MW = 356 g/mol

Polyoxyalkyleneamine (curing agent)

$CH_3CH(NH_2)\text{-}CH[OCH(CH_3)CH_2]_l\text{-}(OCH_2CH_2)_m\text{-}[OCH_2CH(CH_3)]_n\text{-}NH_2$

Jeffamine ED900, ED2003 Avg. MW = 900 or 2003, respectively

Figure 3.5. Chemical structure of epoxy resin and curing agent used to make contact mechanics lenses.

3.2.3. Preparation and Modification of Aluminized Glass

Substrate fabrication entailed sputtering 400 nm of Al (99.999% purity) onto glass microscope coverslips, which yielded an average roughness of 30 Å. They were cleaned with air-plasma for five minutes prior to each experiment. Several of the aluminum oxide substrates were intentionally contaminated with the model organic contaminant by immersing them in a beaker of hexadecane. These slides were subsequently removed from the liquid and were stored vertically.

3.3. Results and Discussion

As is described in the introduction, the principal goal of this study was to demonstrate the feasibility of the JKR contact mechanics technique for probing organic contamination on metal substrates. This was accomplished by measuring the interactions between an epoxy probe and aluminized substrate, both in the presence and absence of hexadecane surface contamination. We performed JKR loading and unloading experiments, and of particular interest was the extent of adhesion hysteresis that resulted upon bringing the epoxy hemisphere into contact with the substrate. As expected, the hexadecane contaminant played a significant role in reducing the adhesion between the higher modulus epoxy system (Dow DER 331/Jeffamine ED-900) and aluminized substrate, as was evident by the significant decrease in adhesion hysteresis (Figure 3.6). This phenomenon was also observed for the lower modulus epoxy system (Dow DER

332/Jeffamine ED-2003), as depicted in Figure 3.7. Once again, trace amounts of hexadecane on the surface resulted in lower adhesion hysteresis in the unloading experiment. As for why the minimum load is often below zero in the presence of the hexadecane contaminant, we believe that this is due to the capillary forces of the liquid residue on the substrate acting on the elastomeric lens. At very low loads, the capillary forces are significant compared with the mechanical force associated with the imposed displacement.

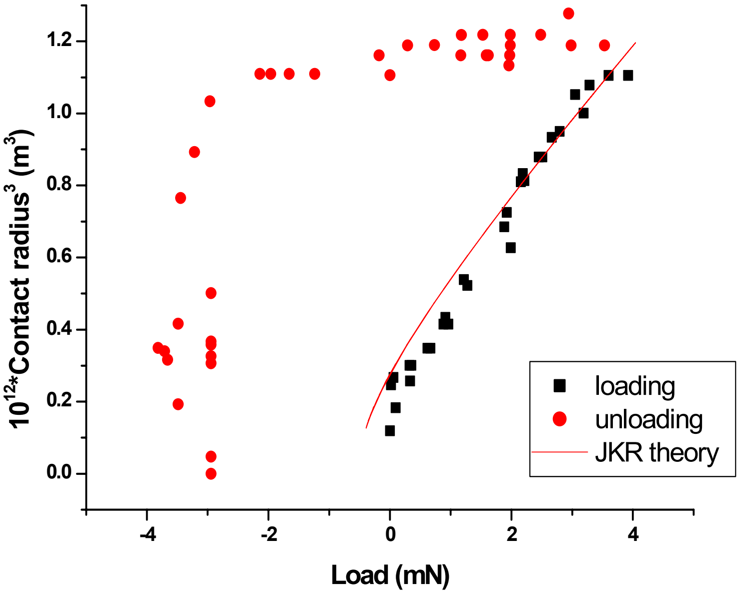

(a)

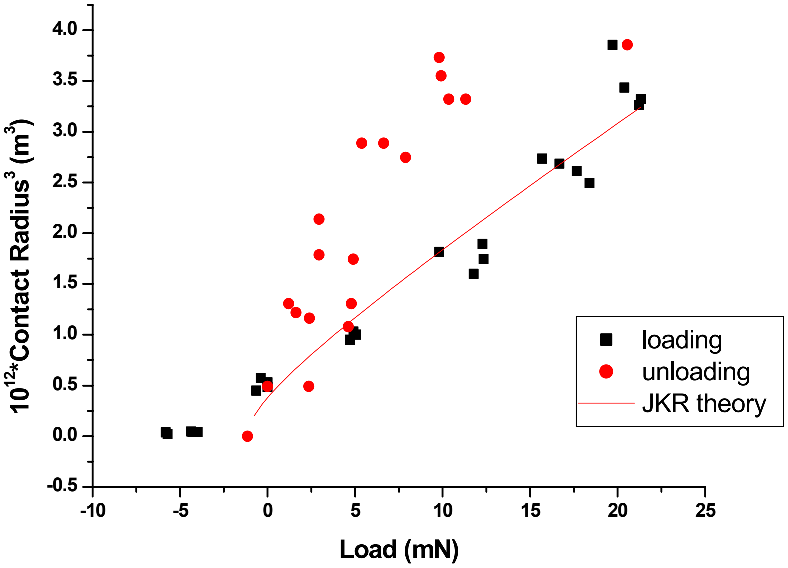

(b)

Figure 3.6. JKR loading and unloading curves of higher-modulus epoxy elastomers in contact with (a) air-plasma cleaned aluminum and (b) hexadecane-contaminated aluminum.

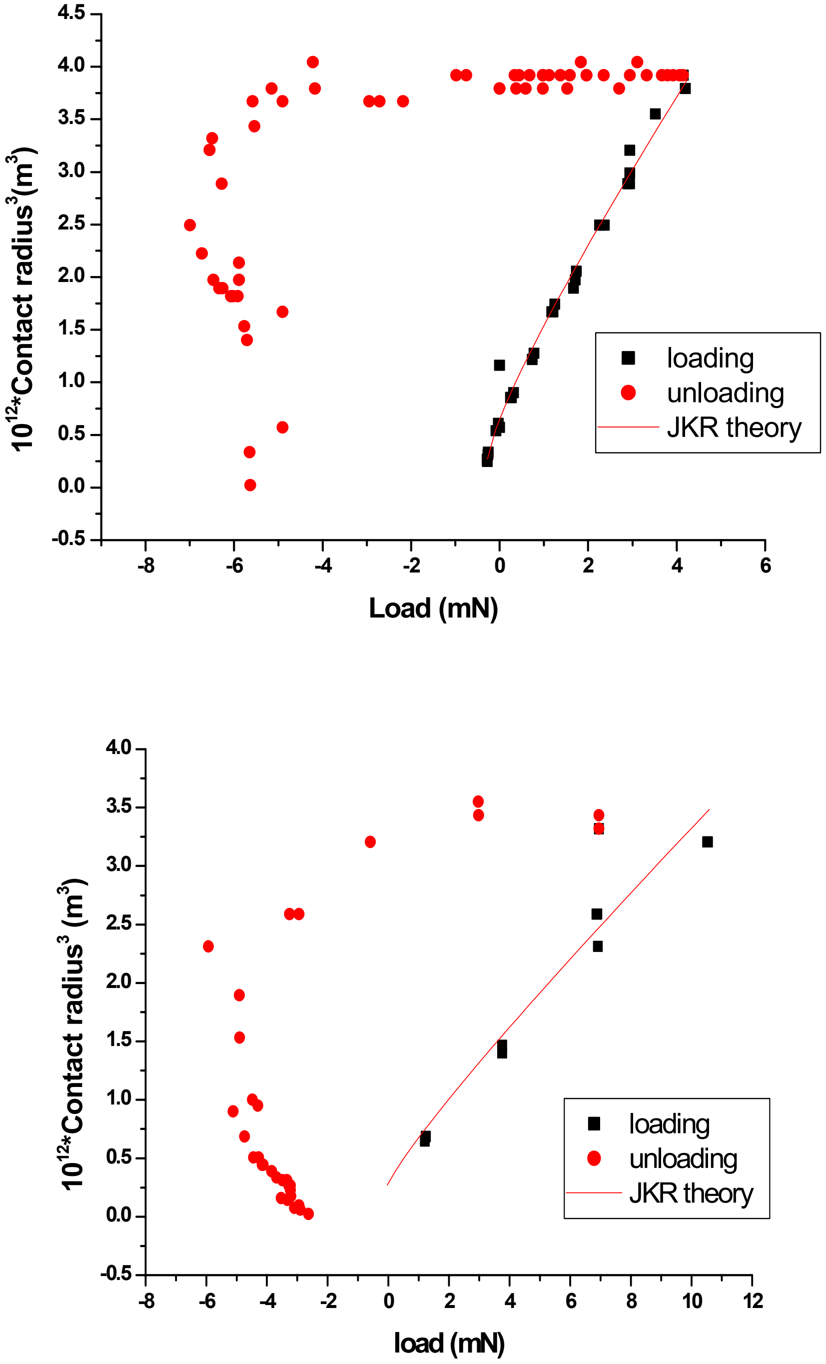

(a)

(b)

Figure 3.7. JKR loading and unloading curves of lower-modulus epoxy elastomers in contact with (a) air-plasma cleaned aluminum, and (b) hexadecane-contaminated aluminum.

3.3.1. Adhesion Hysteresis Parameter

To be able to readily compare levels of contamination on samples of interest, we devised a scheme to extract the information embedded in the adhesion hysteresis curves in a quantitative fashion. Notwithstanding the specific interactions that have evolved inside the contact zone, the area under the unloading curve will depend upon parameters such as the maximum load achieved in the loading experiment (*P_{max}*), as well as the bulk modulus of the lens, *K*. With this in mind, the adhesion energy is computed by first subtracting the area under the loading curve from the area under the unloading curve, which in this particular case, was fitted to two lines, as illustrated in Figure 3.8. This quantity, *H'*, is given by

$$H' = A(q_1 - p_1) + \frac{1}{2}B(q_1{}^2 - p_1{}^2) + C(q_2 - p_2) + \frac{1}{2}D(q_2{}^2 - p_2{}^2)$$

$$- \frac{R}{K}(3\pi WR(q_3 - p_3) + \frac{1}{2}(q_3{}^2 - p_3{}^2) + (9\pi WR)^{-1}(((3\pi WR)^2 + 6\pi WRq_3)^{\frac{3}{2}} -$$

Equation 3.3

$$\left((3\pi WR)^2 + 6\pi WRp_3\right)^{\frac{3}{2}}))$$

where *A* and *C* represent the y-intercepts of the lines, and *B* and *D*, their slopes, and where *p* and *q* represent upper and lower integration limits for each of the three functions, as denoted by the subscripts. *H'* is subsequently normalized with respect to a normalization factor, *N*, where

$$N = P_{\max} \times a^3{}_{\max}$$

Equation 3.4

giving rise to a newly defined adhesion hysteresis parameter, *H*, where

$$H = \frac{H'}{N}$$

Equation 3.5

Calculations of *H* are presented in Table 3.1. Two replicate runs were made for the clean aluminum surface with the low modulus epoxy lens. These two values are very close to each other and very different from the value obtained on the contaminated surface. And with both epoxy systems, *H* was found to be a factor of two or three lower in the presence of the contaminant as opposed to when the contaminant was absent from the surface. With this quantitative distinction between 'clean' and 'contaminated' substrates, one could empirically determine the cutoff point for *H* (*H_c*), below which the bond strength would be adversely affected in a given application. Success of this method hinges on the fact that the surface energy difference between the epoxy elastomer and the model contaminant is large; namely, the surface energy of amine-cured epoxide is 46.2 mJ/m^2 and the surface energy of hexadecane is only 27.6 mJ/m^2.[49]

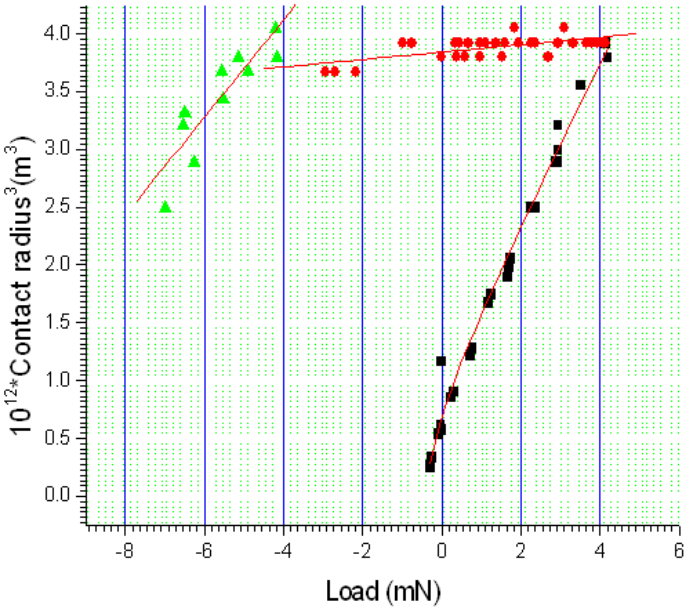

Figure 3.8. Illustration of lines fit to JKR data for calculation of adhesion hysteresis parameter, H.

Table 3.1. Adhesion Hysteresis Parameter, *H*

Epoxy Elastomer	Air-plasma-cleaned aluminum	Hexadecane-contaminated aluminum
DER331/ED-900 epoxy: High modulus system ($K = 9$ MPa, from JKR theory)	1.17	0.383
DER332/ED-2003 epoxy: Low modulus system ($K = 3$ MPa, from JKR theory)	1.68, 1.73	0.867

Alternatively, one has the option of computing the total energy dissipated (U) from experimental and theoretical δ vs. P curves acquired during the loading/unloading cycle,[50] another systematic approach to extracting the hysteresis from the JKR curves. As described previously,[39] the enclosed areas are a direct measure of the total energy dissipated (U) during the hysteresis loop (Equation 3.6)

$$U = \oint P d\delta = -\oint \delta dP$$

Equation 3.6

And we recommend this method for those seeking direct measurements of the elastomer/solid bond strength. However, for a case in which actual energy calculation is not necessary, such as the case where the hemisphere is a representative probe, the method of analyzing the hysteresis directly from the $a^3(P)$ curves rather than from the $\delta(P)$ curves has the advantage that it does not depend on highly accurate values of δ, which are more difficult to achieve than accurate values of a. In our experiment, the percent error in the measurement of a was intrinsically less than the error in the measurement of δ, which was acquired indirectly with a non-contact proximity sensor. Therefore, with regard to sensitivity, one should profit from the analysis of the $a^3(P)$ curves in an industrial application, enabling extremely low levels of surface contamination to be detected.

3.3.2. Significant Surface Contamination

Finally, as an aside we also considered how the adhesive system would behave in the presence of large amounts of hexadecane, that is, when hexadecane residue was actually visible inside the contact area (Figure 3.9). In this particular experiment, a fairly sizable quantity of hexadecane was deliberately left on the substrate after it was immersed in the beaker of hydrocarbon fluid. Figure 3.9 depicts the first two data points of a loading experiment, in which a 1-μm displacement resulted in an increase in the observed area of contact between the lens and substrate (Figure 3.9, left). However, after five minutes the interface had been fractured by the hexadecane, suggesting that in the presence of significant quantities of contamination, W is negative (Figure 3.9, right). A similar event was observed in the work of Hobbs and Kinloch[51] where an adhesive/substrate interface was examined in the presence of water. If one follows their line of reasoning, the interface can be thought of as a three-phase system when hexadecane is present in large quantities giving rise to the revised expression for W:

$$W = 2\gamma_H + W_i - W_{EH} - W_{AH}$$

Equation 3.7

where the subscript H represents the hexadecane environment; EH, the epoxy/hexadecane interface; AH, the aluminum oxide/hexadecane interface; and W_i, the work of adhesion in an inert environment.

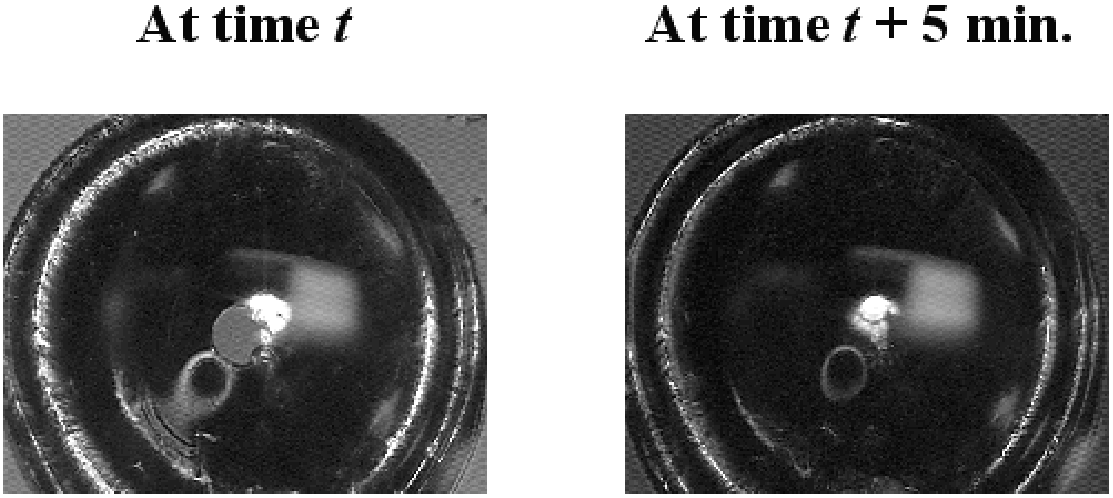
At time *t*

At time *t* + 5 min.

Figure 3.9. Photograph of epoxy lens in contact with a substrate that has been contaminated with a significant amount of hexadecane.

3.4. Summary

The use of JKR contact mechanics for detecting trace amounts of surface contamination has been demonstrated. The approach capitalizes on the difference in surface energy between the epoxy probe and organic contaminant. In particular, we developed a method by which surface cleanliness could be estimated quantitatively by computing an adhesion hysteresis parameter, *H*, defined in this work. The modulus of the elastomeric lens or probe does not appear to interfere with the usefulness of the analysis, providing the engineer with some latitude in implementing this technique in a manufacturing environment. Finally, we have also shown that large amounts of organic contamination will completely disrupt the epoxy probe/metal oxide interface, precluding the use of the JKR contact mechanics technique for probing a three-phase system.

4. Acknowledgments

The authors are grateful to Patrick J. Klein and Mark E. Stavig, who developed the fabrication and testing techniques for the TBNS specimen, and to Prof. David F. Bahr from Washington State University for helping develop and deposit stressed overlayers onto our epoxy samples. We extend a special thanks to Christy Woodcock and Kirsten Schafer from Washington State University for their technical assistance. We thank Stacie Hammerand for developing the spin coating process. We thank Steve Thoma and Duane Schneider for preparing the aluminum processing samples. We thank Dara Woerdeman for her contact mechanics work. We thank Ms. Catharine H. Sifford for preparing the Al-glass substrates and for determining surface roughness. Stimulating conversations with Prof. K. Shull are also acknowledged. The authors also gratefully acknowledge the support of U.S. DOE Contract DE-AC04-94AL85000.

References

[1] Rice, J. R. (1988), *Journal of Applied Mechanics* **55**, 98-103.

[2] Hutchinson, J. W., *Suo*, Z. (1992), *Advances in Applied Mechanics*, (edited by J. W. Hutchinson, T. Y. Wu) Academic Press Inc., New York. NY, **29**, 63-191.

[3] Liechti, K. M., Chai, Y. S. (1992), *Journal of Applied Mechanics* **59**, 295-304.

[4] Liang, Y.-M., Liechti, K. M. (1995), *International Journal of Solids and Structures* **32**, 957-978.

[5] Kuhl, A., Qu, J. (2000), *Journal of Electronic Packaging* **122**, 147-151.

[6] Moody, N. R., Reedy, Jr., E. D., et al. (2002), Sandia National Laboratories.

[7] Kent, M. S., Reedy, Jr., E. D., Stevens, M. J. (2000), *Sandia Report SAND2000-0026*.

[8] Wei, Y., Hutchinson, J. W. (1998), *International Journal of Fracture* **93**, 315-333.

[9] Bagchi, A., Lucas, G. E., Suo, Z., Evans, A. G. (1994), *Journal of Materials Research* **9**, 1734-1741.

[10] Bagchi, A., Evans, A. G. (1996), *Thin Solid Films* **286**, 203-212.

[11] Kriese, M. D., Moody, N. R., Gerberich, W. W. (1998), *Acta materialia* **46**, 6623-6630.

[12] Kriese, M. D., Gerberich, W. W., Moody, N. R. (1999), *Journal of Materials Research* **14**, 3007-3018.

[13] Zhuk, A. V., Evans, A. G., Hutchinson, J. W., Whitesides, G. M. (1998), *Journal of Materials Research* **13**, 3555-3564.

[14] Moody, N. R., Bahr, D. F., Kent, M. S., Emerson, J. A., Reedy, Jr., E. D. (2001) in *Fundamentals of Nanoindentation and Nanotribology II*, (edited by S. P. Baker, R. F. Cook, S. G. Corcoran, and N. R. Moody) Mater. Res. Soc. Proc., Pittsburgh, PA, **649**, Q6.3.1.

[15] Lucas, B. N., Rosenmayer, C. T., Oliver, W. C. (1998), *Thin Films-Stresses and Mechanical Properties VII* (edited by R. C. Cammarata, M. Nastasi, E. P. Busso, W. C. Oliver) Mater. Res. Soc. Proc., Pittsburgh, PA, **505**, 97-102.

[16] Lucas, B. N., Oliver, W. C., Swindeman, J. E. (1998), *Fundamentals of Nanoindentation and Nanotribolgy* (edited by N. R. Moody, W. W. Gerberich, N. Burnham, S. P. Baker) Mater. Res. Soc. Proc., Pittsburgh, PA, **522**, 3-14.

[17] Strojny, A., Moody, N. R., Emerson, J. A., Gerberich, W. W. (2000), *Polymer Systems*, (edited by S. H. Anastasiadis, A. Karim, G. S. Ferguson) Mater. Res. Soc. Proc., Pittsburgh, PA, **629**, F5.13.1-6.

[18] Marsh, D. M. (1963), *Proceedings of the Royal Society A* **279**, 420-435.

[19] Moody, N. R., Kent, M. S., Reedy, Jr., E. D., Bahr, D. F., Emerson, J. A. (2001) in *Proceedings of the 24th Annual Meeting of the Adhesion Society*, (edited by J. A. Emerson) The Adhesion Society, Blacksburg, VA, 309-311.

[20] Moody, N. R., Yang, N., Adams, D. P., Cordill, M. J., Bahr, D. F. (2002), *Polymer Interfaces and Thin Films* (edited by A. Karim, C. W. Frank, T. P. Russell, P. F. Nealy) Mater. Res. Soc. Proc., Pittsburgh, PA, **710**, DD10.6.1-6.

[21] Adams, D.P., Bahr, D. F., Private Communication. Work done for PECASE LDRD, project #35376, Sandia National Laboratories, Albuquerque, NM 87185.

[22] Marshall, D. B., Evans, A. G. (1984), *Journal of Applied Physics* **56**, 2632-2638.

---

[23] Evans, A. G., Hutchinson, J. W. (1984), *International Journal of Solids and Structures* **20**, 455-466.

[24] Tvergaard, V., *Hutchinson*, J. W. (1993), *Journal of the Mechanics and Physics of Solids* **41**, 1119-1135.

[25] Volinsky, A. A., Gerberich, W. W. (1999), *Materials Reliability in Microelectronics IX* (edited by C. A. Volkert, A. H. Verbruggen, D. Brown) Mater. Res. Soc. Proc., Pittsburgh, PA, **563**, 275-284.

[26] Suo, Z., Hutchinson, J. W. (1989), *Material Science and Engineering* **A107**, 135-143.

[27] Emerson, J. A., Guess, T. R., Adkins C. J., Curro J. C., Reedy, Jr., E. D., Lopez E. P., and Lemke P. (2000) Investigation of the Impact of Cleaning on the Adhesive Bond and the Process Implications, SAND Report 2000-1042.

[28] Schweizer, K. S., Curro, J. G. (1987) *Phys Rev Lett* **58**, 246.

[29] Curro, J. G., Schweizer, K. S. (1987) *Macromolecules* **20,** 1928 and *J Chem Phys* **87**, 1842.

[30] Schweizer, K. S., Curro, J. G. (1997) *Adv Chem Phys* **98**, 1.

[31] Fink, B. K., McCullough, R. L. (1999) *Composites, Part A: Applied Science & Manufacturing* **30(1)**, 1-2.

[32] Shanahan, M. E. R. (2000) *J Colloid Interface Sci* **229**, 168.

[33] Johnson, K. L., Kendall, K., Roberts, A. D. (1971) *Proc. R. Soc. London: Part A* **324**, 301.

[34] Chaudhury, M. K., Whitesides, G. M. (1991) *Langmuir* **7**, 1013.

[35] Brown, H. R. (1993) *Macromolecules* **26**, 1666.

[36] Silberzan, P., Perutz, S., Kramer, E. J., Chaudury, M. K. (1994) *Langmuir* **10**, 2466.

[37] Creton, C., Brown, H. R., Shull, K. R. (1994) *Macromolecules* **27**, 3174.

[38] Deruelle, M., Léger, L., Tirrell M. (1995) *Macromolecules* **28**, 7419.

[39] Ahn, D., Shull, K. R. (1996) *Macromolecules* **29**, 4381.

[40] Shull, K. R., Ahn, D., Mowery, C. L. (1997) *Langmuir* **13**, 1799-1804.

[41] Chin, P., McCullough, R. L., Wu, W. L. (1997) *J Adhesion* **64**, 145-160.

[42] Choi, G. Y., Kim, S., Ulman, A. (1997) *Langmuir* **13**, 6333-6338.

[43] Briscoe, B. J., Liu, K. K., Williams, D. R. (1998) *J Colloid Interface Sci* **200**, 256-264.

[44] Deruelle, M., Hervet, H., Jandeau, G., Léger, L. J. (1998) *Adhes Sci Technol* **12**, 225-247.

[45] Woerdeman, D. L., Amouroux, N., Ponsinet, V., Jandeau, G., Hervet, H., Léger, L. (1999) *Composites Part A: Applied Science & Manufacturing* **30(1),** 95-109.

[46] Rundlöf, M., Karlsson, M., Wågberg, L., Poptoshev, E., Rutland, M., Claesson, P. (2000) *J Colloid Interface Sci* **230**, 441-447.

[47] Falsafi, A., Tirrell, M., Pocius, A. V. (2000) *Langmuir* **16**, 1816-1824.

[48] Hertz, H. *Gesammelte Werke*, Leipzig, 1895.

[49] Comyn, J. (1997) *Adhesion Science, The Royal Society of Chemistry* 107-112.

[50] Shull, K. R. (2001) Private Communication.

[51] Hobbs and Kinloch (1998) *J. Adhesion* **66**, 203-228.

5. Appendix A. Validation of the method used to insert an initially sharp crack

Initial attempts to simply use an ODTS SAM coating on the aluminum surface to introduce a weak interface (G_c~2 J/m^2) for a crack-starter were not successful. Although the portion of the interface with the ODTS SAM has a very low toughness, the load required to open the coated region was higher than that needed to propagate a crack with a length equal to the coated region. This is undoubtedly a common problem when attempting to insert a pre-crack using a low adhesion coating. Even though weakly bonded, it is still difficult to open an intact interface. Furthermore, it is difficult to ascertain if the weakly bonded region is opening up in the desired manner unless the specimen is suitably instrumented when cracking is unstable. After some experimentation, an approach that places a Teflon tape over an ODTS SAM coating that extends beyond the tape to define a sharp crack tip was found to work. Figure 5.1 shows measured load vs. load-point displacement for two TBNS specimens that had a crack starter composed of a 23-mm long ODTS SAM and either a 15-mm or 20-mm Teflon tape applied on top of the SAM (i.e., the SAM extended 8 and 3-mm, respectively, beyond the tape). The interface between the tape and the epoxy initially remained intact, and then the load-point displacement abruptly jumped as the interface opened up to the end of the SAM. Upon further loading, the opened crack ultimately propagates unstably and the specimen fails. Note that even though two different tape lengths were used, both arrested at the same load-point displacement. In this study, specimens were pre-cracked by first loading them to about 75% of the load required to fail the specimen, and then holding the load fixed, typically for about one minute, until the interface opened (Figure 5.2). The two loading-holes closest to the crack plane were used to load the specimen since this mode 1-like loading produces the required G level at a relatively low applied force.

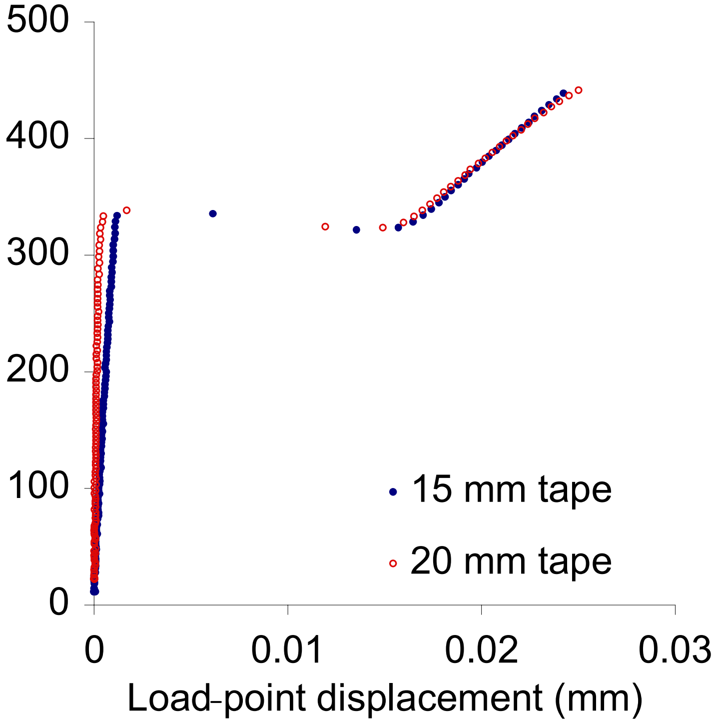

Figure 5.1. Load vs. load-point displacement for two TBNS specimens that had a crack starter composed of a 23-mm ODTS SAM and either a 15-mm or 20-mm long Teflon tape applied on top of the SAM.

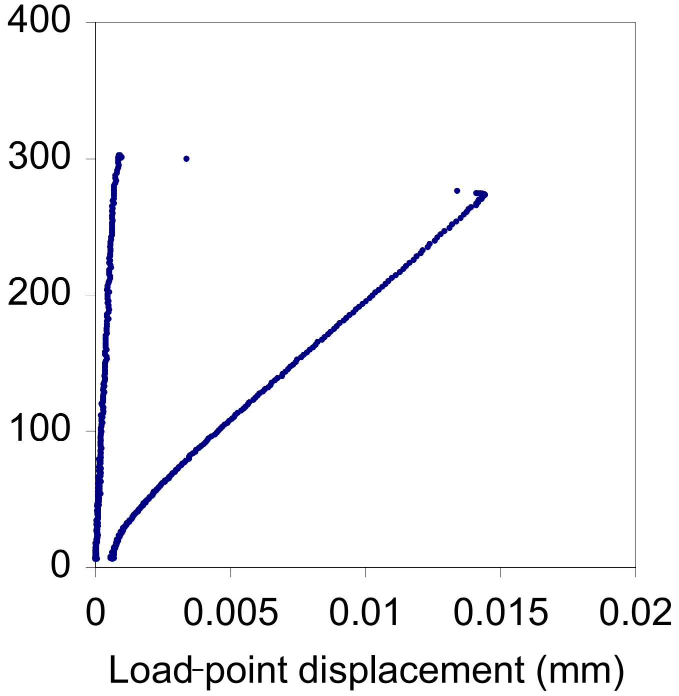

Figure 5.2. Load vs. load-point displacement measured during the pre-cracking of a TBNS specimen (load held fixed at about 75% of the failure load until the interface opens).

6. Appendix B. G calibration for the TBNS specimen

Preliminary finite element calculations for the TBNS specimen showed that the common approach for analyzing a sandwich specimen as a homogeneous material and then applying a correction to account for the presence of a relatively thin bond[26] is not accurate for the aluminum adherend, epoxy-bonded TBNS specimen. For example, the calculated *G* for a 20° diametral loading of a TBNS specimen with aluminum adherends is reduced by a third when the elastic properties of the specimen's 0.5-mm bond are changed from those corresponding to epoxy to those corresponding to aluminum (i.e., changed to a homogeneous aluminum specimen). This is presumably attributable to the bending-like deformation generated in the specimen's intact ligament and the sensitivity of this global deformation mode to the bond's compliance. Other test calculations showed the importance of applying the loads at the loading-hole location, and not simply on the outer diameter. For these reasons, a previously published calibration for the TBNS specimen[5] was not used. Instead, a new calibration was developed based upon a detailed plane strain finite element analysis that explicitly modeled the TBNS specimen's 0.5-mm thick epoxy bond and applied loads at the actual loading-hole positions.

The TBNS specimen calibration used in this study is defined by the relationship

$$G = \left(\frac{P}{W}\right)^2 \frac{\left(1-\beta^2\right)}{\hat{E}R} f\left(\frac{a}{R},\frac{h}{R},\frac{R_L}{R},\alpha,\beta,\theta\right)$$

Equation 6.1

where P is applied load, W is specimen width, R is specimen radius, R_L is radius at loading-hole position, a is crack length, h is adhesive thickness, θ is loading angle (Figure 1.1, defined by the position of the loading-hole in the upper adherend), and α and β are Dundurs' elastic mismatch parameters for plane strain with

$$\alpha = \frac{\overline{E}_1 - \overline{E}_2}{\overline{E}_1 + \overline{E}_2}$$

Equation 6.2

$$\beta = \frac{1}{2}\frac{\mu_1(1-2\nu_2)-\mu_2(1-2\nu_1)}{\mu_1(1-\nu_2)+\mu_2(1-\nu_1)}$$

Equation 6.3

$$\frac{1}{\hat{E}} = \frac{1}{2}\left(\frac{1}{\overline{E}_1}+\frac{1}{\overline{E}_2}\right) \text{ and } \overline{E}_i = \frac{E_i}{1-\nu_i^2} \; for\, i = 1,2$$

Equation 6.4

E_i, μ_i, and ν_i are Young modulus, shear modulus, and Poisson's ratio, respectively, of the aluminum adherends (i=1) and the epoxy adhesive (i=2). Figure 6.1 plots and provides curve fits for the nondimensional function f for a diametrally-loaded aluminum/epoxy TBNS sample ($h/R=0.02$, $R_L/R=0.8$, $\alpha=0.90$, $\beta=0.21$) as a function of a/R and θ while Figure 6.2 plots f vs. θ for $a/R=0.91$(the crack length used in this study). As indicated in Figure 6.2, when $a/R=0.91$ the mode mixity $\psi_{r=h}$ equals -57°, -41°, -27°, -13°, 2°, 16°, and 31° for a diametral loading of θ= -60°, -40°, -20°, 0°, 20°, 40°, and 60°, respectively. Note that $\psi_{r=h}$ does exhibit a modest dependence on crack length. For example, when $a/R=0.50$, $\psi_{r=h}$ equals -56°, -47°, -33°, -14°, 6°, 21°, and 31° for a diametral loading of θ = -60°, -40°, -20°, 0°, 20°, 40°, and 60°, respectively. Figure 6.3 presents results for a symmetric loading that uses the two loading-holes closest to the crack plane (i.e., +/-30° from the crack plane, with $\psi_{r=h}$ equals -13°).

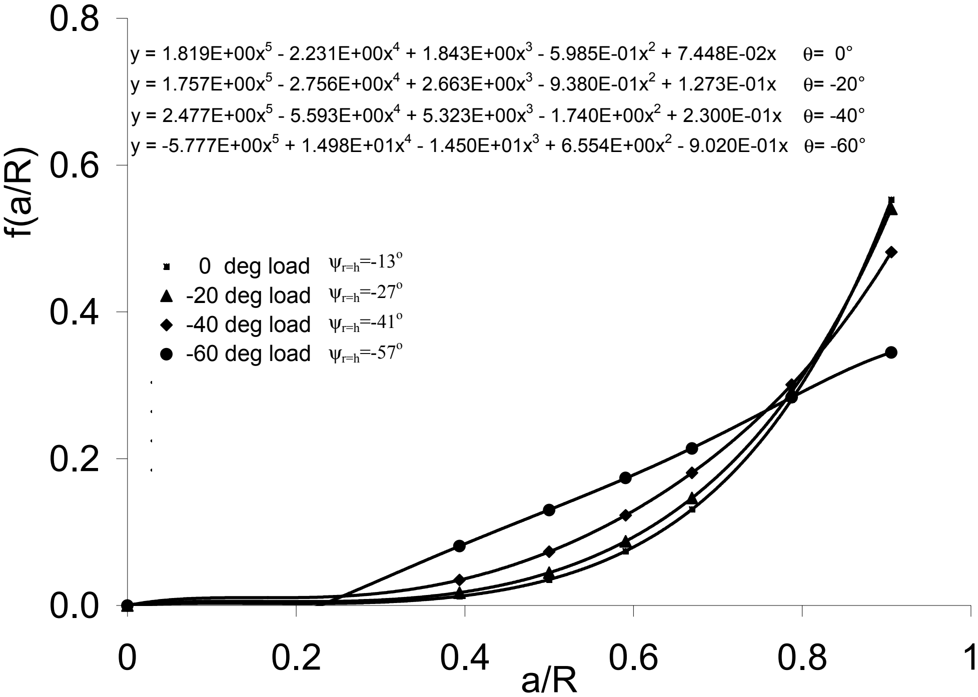

Figure 6.1. Nondimensional *G* calibration function *f* for a diametrally-loaded aluminum/epoxy TBNS specimen (h/R=0.2, $R_L/R=0.8$, α=0.90, β=0.21) as a function of *a/R* and θ (in curve fits, x=*a/R* and y=*f*).

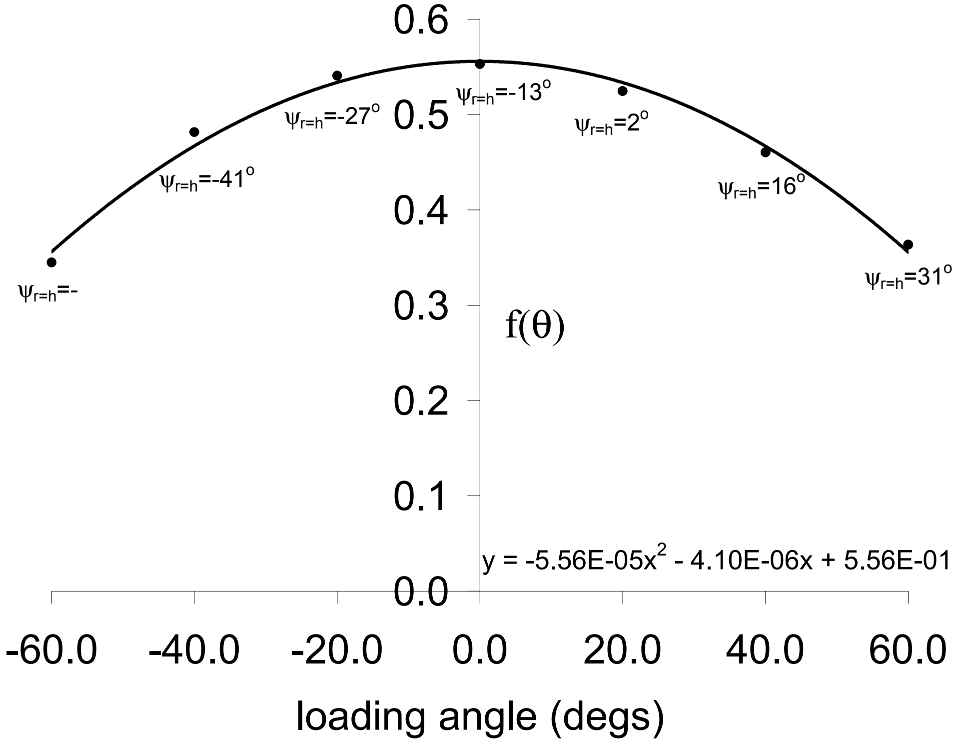

Figure 6.2. Nondimensional *G* calibration function *f* for a diametrally-loaded aluminum/epoxy TBNS specimen (h/R=0.02, a/R=0.91, R_L/R=0.8, α=0.90, β=0.21) as a function of and θ (in curve fits, x=θ and y=*f*).

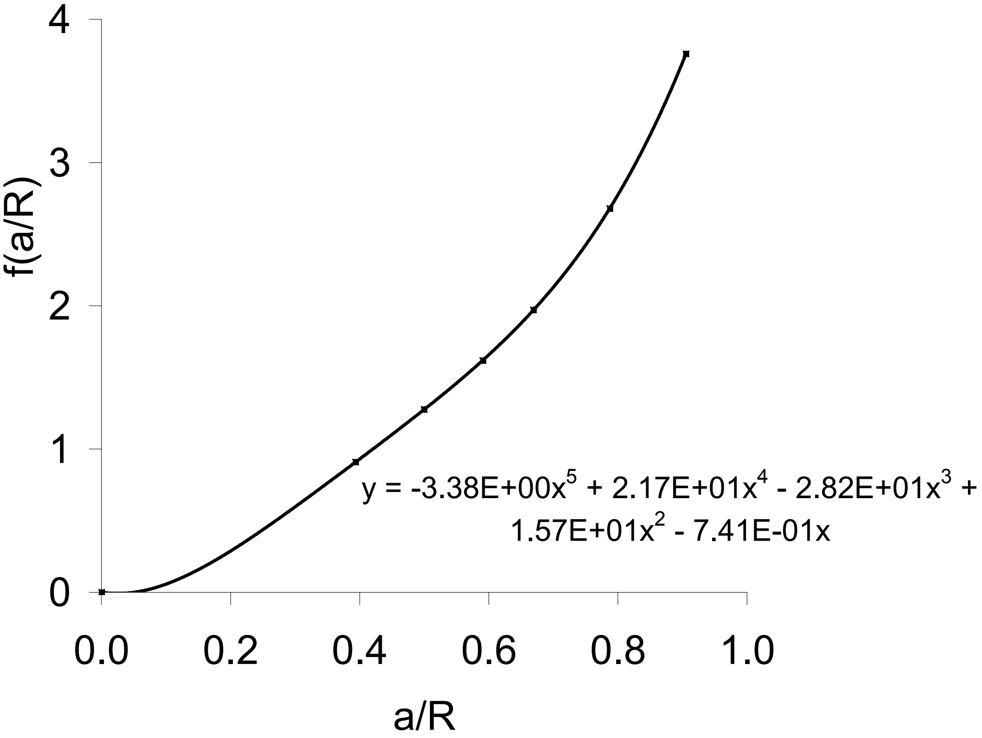

Figure 6.3. Nondimensional *G* calibration function *f* for the +/30° loading about the crack plane (a/R=0.0197, R_L/R=0.8, α=0.90*,* β=0.21) as a function of *a/R* (in curve fits, x=*a/R* and y=*f*).

Distribution:

1	MS	0188	LDRD office
1		0893	E. D. Reedy, 9123
1		0893	J. Pott, 9123
1		0958	R. K. Giunta, 14172
6		0958	J. A. Emerson, 14172
1		0958	J. A. Ruffner, 14172
1		0959	D. P. Adams, 14171
1		0960	Paul A. Lemke, 14100
1		0961	C. L. J. Adkins, 14100
6		9404	N. R. Moody, 8725
1		9404	J. R. Garcia, 8725
1		9018	Central Technical Files, 8945-1
2		0899	Technical Library, 9616
1		0612	Review & Approval Desk, 9612 For DOE/OSTI